

# Functional hyperemia drives fluid exchange in the paravascular space

**Ravi Kedarasetti**

Pennsylvania State University University Park : Penn State <https://orcid.org/0000-0003-4226-5683>

**Kevin L. Turner**

Pennsylvania State University University Park : Penn State

**Christina Echagarruga**

Pennsylvania State University University Park : Penn State

**Bruce J. Gluckman**

Pennsylvania State University University Park : Penn State

**Patrick J. Drew** (✉ [pjd17@psu.edu](mailto:pjd17@psu.edu))

<https://orcid.org/0000-0002-7483-7378>

**Francesco Costanzo**

Pennsylvania State University University Park : Penn State

---

## Research

**Keywords:** Functional hyperemia, paravascular space, fluid exchange

**Posted Date:** June 12th, 2020

**DOI:** <https://doi.org/10.21203/rs.3.rs-22610/v2>

**License:**   This work is licensed under a Creative Commons Attribution 4.0 International License. [Read Full License](#)

---

**Version of Record:** A version of this preprint was published on August 20th, 2020. See the published version at <https://doi.org/10.1186/s12987-020-00214-3>.

# Abstract

The brain lacks a conventional lymphatic system to remove metabolic waste. It has been proposed that fluid movement through the arteriolar paravascular space (PVS) promotes metabolite clearance. We performed simulations to understand how arteriolar pulsations and dilations, and brain deformability affect PVS fluid flow. In simulations with compliant brain tissue, arteriolar pulsations did not drive appreciable flows in the PVS. However, when the arteriole dilated as in functional hyperemia, there was a marked movement of fluid. Simulations suggest that functional hyperemia may also serve to increase fluid exchange between the PVS and the subarachnoid space. We measured blood vessels and brain tissue displacement simultaneously in awake, head-fixed mice using two-photon microscopy. These measurements showed that brain deforms in response to pressure changes in PVS, as predicted by simulations. Our results show that the deformability of the brain tissue needs to be accounted for when studying fluid flow and metabolite transport.

Acknowledgements: This work was supported by NSF Grant CBET 1705854.

## Introduction

The brain is surrounded by cerebrospinal fluid (CSF), and the movement of CSF can transport metabolic waste out of the brain<sup>1-7</sup>. The nature of CSF movement into the brain tissue (where it might exchange solutes and fluid with interstitial fluid, ISF) has been a source of controversy<sup>8-15</sup>. Recent work<sup>16,17</sup> has suggested directional CSF movement along the paravascular space (PVS) around arterioles. The PVS is a fluid-filled region between the arteriolar smooth muscle and astrocyte endfeet, and it is connected to the subarachnoid space (SAS). The bulk movement of CSF is thought to be driven by heart beat-driven pulsations of arterioles, which pump CSF through the PVS (“peristaltic pumping”) <sup>16,18,19</sup>. Because the PVS extends into the brain parenchyma, the conservation of fluid mass (continuity equation of fluid dynamics) dictates that directional flow in the PVS implies bulk flow of fluid in the parenchyma<sup>16,20</sup>. However, several studies have given a conflicting view, claiming that there is no bulk fluid movement in the parenchyma, and that transport in the brain parenchyma is due to diffusion<sup>10,12,14,21,22</sup>. While the existence bulk fluid flow in brain parenchyma is controversial, there is clear agreement that there is bulk flow of CSF through the SAS, and that CSF exits from the cranial space through pathways in the dural sinuses, the base of the skull, or the cribriform plate<sup>1-7,23,24</sup>. The bulk flow of CSF in the SAS is believed to be driven by CSF secretion from the choroid plexus<sup>25</sup> and by transient changes in the brain tissue volume induced by the cardiac cycle<sup>26</sup> and respiration<sup>27</sup>.

An important approach for understanding fluid movement in the brain and the PVS is simulation of fluid dynamics. Calculations based on fluid mechanics<sup>13,19,28</sup> do not agree on the magnitude and direction of the proposed “peristaltic pumping” mechanism. Moreover, the previously published models have treated the brain tissue as a non-compliant solid for simplicity<sup>11,13,14,19</sup>. In reality, brain tissue is very compliant<sup>29-32</sup> (‘soft’), with a shear modulus in the range of 1-8kPa. Given the compliant nature of the brain, even relatively small pressure changes will cause deformations of the tissue and would consequently produce fluid movements very different from those that would occur if the brain were non-compliant. While the deformability of the brain tissue has been shown to effect several aspects of the CSF flow<sup>26,33-37</sup>, to the best

of our knowledge, ours is the first model to investigate the effect of brain deformability on the flow in the PVS.

In this study, we used finite element simulations to model fluid exchange between the PVS and the SAS. The anatomical regions of interest in our calculations include the cerebral arterioles, the PVS, the brain tissue and the SAS (Fig 1A). In our models, we have two contiguous fluid-filled compartments, namely the PVS and the SAS. Several experimental and modeling studies<sup>12,14,21,38</sup> suggest that there is no appreciable fluid flow in the brain tissue and that metabolite transport in the brain occurs through diffusion. Consistent with these experimental results, we modeled the brain as a solid with no fluid flow through the tissue. To make the calculations and interpretation of results simpler, we assume a cylindrically symmetric geometry with the centerline of the arteriole as the axis of symmetry (Fig 1B). We performed fluid-structure interaction simulations that couple the mechanics of fluid movement in the PVS and the solid mechanics of the brain tissue. Our simulations suggest that arteriolar pulsations cannot drive appreciable movement of CSF in the PVS. Our simulations also suggest that neural activity-driven functional hyperemia can drive large fluid exchange between the PVS and the SAS, improving metabolite clearance from the brain. These models predicted arteriole dilation-induced deformation of the surrounding brain tissue, which we experimentally verified in awake mice. These results suggest that in addition to its involvement in other processes, functional hyperemia can drive the exchange of CSF between the SAS and PVS.

## Results

We first explain our modeling choices and parameters before diving into the results of our simulations. We are interested in understanding how the motions of the arteriolar walls drive fluid exchange between the PVS and SAS. We performed fluid mechanics simulations of the CSF in the PVS surrounding penetrating arterioles in adult mice. There is great deal of ambiguity regarding several key parameters governing the fluid flow of the PVS, namely the permeability of the PVS, channel width of the PVS, and the flow resistance of the surrounding spaces (the brain parenchyma and the SAS). These ambiguities pertaining to flow in the PVS within the subarachnoid space<sup>20</sup> and the parenchyma<sup>39</sup> are discussed in detail in recent reviews on the subject. Keeping these ambiguities in mind, we performed simulations for a wide range of parameters (see Table 1) to ensure that our results are robust (Fig S9).

---

Table 1 | Parameters used in simulations

Parameter Name	Symbol	Default	Range	Unit	Source
Arteriolar radius	$R_1$	12	5 to 20	$\mu\text{m}$	40-42
PVS length	$L_a$	250	250 to 500	$\mu\text{m}$	41,43
PVS width	wd	3	2-10	$\mu\text{m}$	16,44,45
CSF viscosity	$\mu_f$	0.001	-	Pa.s	46,47
CSF Density	$r_f$	1000	-	$\text{kg}/\text{m}^3$	46,47
PVS porosity	z	0.8	0.5-0.9	-	16,17,48
PVS permeability	$k_s$	$2 \times 10^{-14}$	$7 \times 10^{-13}$ to $2 \times 10^{-15}$	$\text{m}^2$	12,14,49,50
Brain section radius	$R_3$	150	100-200	$\mu\text{m}$	43,51
Brain shear modulus	$\mu_s$	4	1-8	kPa	29-32,52-55
Brain tissue density	$r_s$	1000	-	$\text{kg}/\text{m}^3$	56
Pulsation amplitude (% arteriolar radius)	$b_1$	1	0.5-2	-	16
Pulsation Frequency	f	10	7-14	Hz	57
Pulse wave speed	c	1	0.5-10	m/s	58-60
Pulse wave wavelength	l	0.1	0.03-1.43	m	c/f
Diffusion coefficient	D	$1.4 \times 10^{-6}$	-	$\text{cm}^2/\text{s}$	61,62

We posit that fluid movement in the PVS is governed by the Darcy-Brinkman<sup>63</sup> equations (one for the momentum balance and the other for volume conservation), which is used to simulate flow through highly porous regions<sup>64</sup>. This choice is based on the experimental data available from recent studies that used intra-cisternal infusions to study the flow of CSF. These studies have shown unobstructed movement of 1  $\mu\text{m}$  particles in the PVS surrounding arterioles on the surface of the brain<sup>16,17</sup>. While these relatively large particles do not enter the PVS surrounding penetrating arterioles, dye-conjugated dextrans (3-500 kDa) with a hydrodynamic radius of 1-15 nm<sup>65</sup> travel preferentially through the PVS of the penetrating arterioles<sup>44,45,66</sup>. Based on these results, we modeled the PVS surrounding penetrating arterioles as a porous medium with higher porosity and fluid permeability than the brain tissue. The porosity (fraction of fluid volume to the total

volume) of the PVS was assumed to be between 0.5-0.9. The fluid permeability of the PVS is taken from a range of possible values. The minimum value of PVS permeability we used was  $2 \times 10^{-15} \text{ m}^2$ , the measured permeability of the brain tissue<sup>49,50</sup>. We also performed simulations with infinite permeability, where the Darcy-Brinkman equations recover the standard Navier-Stokes equations that govern flow in an open channel. The default value of permeability was taken to be  $2 \times 10^{-14} \text{ m}^2$ , where the PVS is 10 times more permeable than the brain parenchyma. This was chosen because dye injected through the cisterna magna enters the PVS (< 5 mins) nearly 10 times faster than it enters the parenchyma (~30 mins)<sup>45</sup>. The viscosity (0.001 Pa\*s) and density (1000 kg/m<sup>3</sup>) of CSF were taken from experimentally determined values<sup>46,47</sup>.

The PVS is assumed to be 150-300  $\mu\text{m}$  long and 2-10  $\mu\text{m}$  wide for an arteriolar radius of 5-20  $\mu\text{m}$ <sup>40-42</sup>. The length of 150-300  $\mu\text{m}$  is in the range of bifurcation free length of penetrating arterioles in the mouse parenchyma. This is consistent with the length of the PVS used in previous studies that used an axisymmetric model of the PVS surrounding penetrating arterioles<sup>13</sup>. While the PVS surrounding large pial arterioles is in the range of 20-40  $\mu\text{m}$ <sup>16,17</sup>, the PVS around penetrating arterioles appears to be much smaller (this is clearly evident in Fig 6c of Schain *et al.* (2017)<sup>44</sup>). The width of this section of the PVS is not explicitly mentioned in the literature. However, a width of 2-10  $\mu\text{m}$  can be calculated from the imaging data available from experimental studies<sup>44,45</sup>.

In the cerebral cortex of mice, the fluid leaving the PVS around penetrating arterioles has to enter the SAS or the PVS around pial arterioles on the pial side (green arrows in Fig 1a) or the brain parenchyma or the para-capillary and para-venous spaces on the other side (magenta arrows in Fig 1a). To avoid confusion, we refer to the first set of fluid chambers as the SAS and the second set as the parenchyma. Due to the relatively large PVS surrounding the pial vessels<sup>16,17</sup>, the SAS region has a relatively low flow resistance compared to the PVS. Therefore, in our models the pial opening of the PVS is connected to a flow resistance with a resistance value 1/100<sup>th</sup> of the flow resistance of the PVS. The parenchyma is assumed to have a higher flow resistance, 10 times that of the PVS. There is evidence suggesting the anatomy and therefore the flow path of CSF is more complicated than what we modelled here. Potter *et al.*<sup>67,68</sup> showed that the PVS might be very small or non-existent in the healthy brain. Albargothy *et al.*<sup>69</sup> showed that CSF in the paraarterial space mostly likely flows out through the periaarterial basement membrane and not out of the paravenous space. There is also evidence showing that the PVS and the SAS are not contiguous fluid filled compartments but are connected through the stomata or pores in the leptomeningeal cell layer surrounding arterioles<sup>38,70</sup>. Even though our assumptions do not exactly match these findings, the path of least resistance for the flow of CSF seems to be through the SAS and around penetrating arterioles<sup>38,67-70</sup>, which is captured in our model.

We did not model fluid flow into the brain parenchyma, either through possible gaps in the glia limitans surrounding arterioles<sup>71</sup> or through the aquaporin channels in the astrocytic endfeet<sup>45,72,73</sup>, because there is no agreement on the existence of bulk flow in the brain parenchyma<sup>8,10-12,14,16,73</sup>. Models that have simulated the flow through astrocytic endfeet and the brain extracellular space concluded that transport through these pathways is dominated by diffusion and not bulk flow<sup>11,14</sup>. This is a limitation of our model, and our calculations of net flow into the brain need to be interpreted with this limitation in mind. Instead of

the controversial bulk flow through the brain, we use the well-established CSF flow through the SAS<sup>1,2,5-7,23-27</sup> as the basis for metabolite clearance from the PVS. We hypothesized that the fluid exchanged between the SAS and the PVS could be carried away by the existing directional flow in the SAS and aid clearance of metabolites from the PVS. In order to quantify the fluid exchanged between the PVS and SAS, we quantified the volume exchange fraction,  $Q_f$ , driven by arteriolar wall movement. The volume exchange fraction is defined as the ratio of the maximum amount of fluid leaving the PVS to the total volume of fluid in the PVS (see appendix for full mathematical definition). We use the volume exchange fraction as the metric for the fluid exchange between the SAS and the PVS and metabolite clearance from the PVS (Figs S9, S11). The transfer of metabolites from the brain interstitial space to the PVS is not explicitly modelled here, and is assumed to occur via diffusion<sup>10,12,14,21,22</sup>.

In models where we simulate the brain tissue as a deformable solid, the brain tissue was modelled as a compressible, Saint-Venant-Kirchhoff solid. A Poisson's ratio of 0.45 was chosen, as it best describes the mechanical response of brain tissue under compression<sup>74</sup>. We also performed these simulations with an incompressible Neo-Hookean elastic model for the brain tissue. These Saint-Venant-Kirchhoff and Neo-Hookean models are chosen to minimize the number of model parameters. These models have been shown to accurately estimate brain tissue deformation during craniotomies and automated surgeries<sup>75,76</sup>. The elastic (shear) modulus of the brain tissue was taken to be between 1-8 kPa, spanning the values found in the literature<sup>31,32,52-55</sup>. The radius of the simulated section of brain tissue was taken to be in the range of 100-200  $\mu\text{m}$ , half of the typical distance between two penetrating arterioles in the mouse cortex<sup>77,78</sup>. In the models where the deformability of the tissue is modelled, we saw that the pressure changes in the PVS can cause deformation in the brain and affect fluid flow in the PVS (Fig S6). To model the pressure changes on the pial surface of the brain more accurately, we repeated our simulations where the flow resistance model at the pial opening of the PVS was replaced with a fluid filled SAS connected to the PVS over the brain surface (Supplementary figures S5, S8).

The dilations caused by heartbeats and in response to local neural activity have very different temporal dynamics and amplitudes. Heartbeat drives changes of 0.5-3% in the radius of pial arterioles in mice<sup>16</sup>. These pulsations travel at a speed of 0.5-10 m/s along the arterial tree<sup>58-60</sup>. Mice have a heart rate of 7-14 Hz when they are unanaesthetized and freely behaving<sup>57</sup>. Neural activity can drive 10-30% changes in arteriolar radius<sup>42,79</sup>. Neural activity-driven changes in arteriolar diameter take place at a nominal frequency range of 0.1-0.3 Hz<sup>57</sup>.

### **Ignoring brain deformability leads to implausibly high pressures**

We first investigated the hypothesis that heartbeat-driven pulsations propagating through the arteriolar wall can pump CSF into the brain<sup>19,28,80</sup> (peristaltic pumping). In this model, the space between the penetrating arteriole (the inner wall of the PVS) and the brain (the outer wall of the PVS) is filled with fluid. Fluid enters or exits the PVS through the SAS or the parenchyma (Fig 1a). The flow resistance of the SAS was 0.01 times the flow resistance of the PVS. The flow resistance of the parenchyma was 10 times that of the PVS. To quantify the flow driven by peristalsis alone, we imposed no pressure difference across the two ends of the

PVS. Consistent with the assumption that the brain tissue is non-compliant, the position of the outer wall of the PVS was fixed (as was done in other models<sup>13,19</sup>). The balance laws and boundary conditions are described in methods. To simulate the peristaltic wave due to the heartbeat, the position of the inner wall of the PVS was prescribed via a travelling sinusoidal wave whose amplitude<sup>16</sup>, frequency<sup>57</sup> and velocity<sup>58,59</sup> were taken from experimental observations in mice. The results of the simulation with Darcy-Brinkman model are shown in Fig 2 and Navier-Stokes model are shown in Fig S1.

When the dimensions of the PVS in the simulations was of anatomically realistic size (3  $\mu\text{m}$  wide and 250  $\mu\text{m}$  long), we observed no appreciable net unidirectional movement of fluid. The average downstream velocity of fluid was  $5.5 \times 10^{-4} \mu\text{m/s}$  ( $1.84 \times 10^{-3} \mu\text{m/s}$  for Navier Stokes model) with an average flow rate of  $0.14 \mu\text{m}^3/\text{s}$  ( $0.47 \mu\text{m}^3/\text{s}$  for Navier Stokes). Instead, we see periodic fluid movement in and out of PVS (Fig 2b) with peak velocity magnitude in the range of  $300 \mu\text{m/s}$  (Reynolds number,  $\text{Re} = 1.3 \times 10^{-3}$ ), resulting in an oscillatory flow with negligible net unidirectional movement. We also repeated the simulation without the flow resistances (Fig S2) and found an average downstream velocity of  $2.95 \times 10^{-3} \mu\text{m/s}$ . There was essentially no net fluid movement in these conditions because the wavelength of the cardiac pulsation (0.1 m in mice, see table 1) is much longer than the PVS (150-300  $\mu\text{m}$ ). When the wavelength of the pulsation is substantially larger than the length of the PVS, the arteriolar wall movement cannot capture the shape of the peristaltic wave on the scale of cerebral arterioles. Effectively, the entire length of arteriolar wall moves in or out almost simultaneously. This effect can be better understood by comparing the arteriolar wall movement in a 250  $\mu\text{m}$  arteriole (Fig S2) with a 0.1 m arteriole (Fig S3).

Our results are very similar, in terms of magnitude and direction of fluid velocities (Fig 2b), to those obtained by Asgari *et al*<sup>13</sup>, who used a similar PVS geometry in their model. Asgari *et al*<sup>13</sup> showed that large oscillatory fluid flow in the PVS can promote fluid mixing within the PVS and in between the PVS and the SAS and thus improve metabolite transport. When we simulated a PVS 0.1 m in length, we saw pumping of fluid, consistent with Wang and Olbricht<sup>19</sup>, and Schley *et al*<sup>8</sup> with an average downstream speed of  $143.2 \mu\text{m/s}$ . However, these models predict pressure differences of up to  $2.0 \times 10^5 \text{ mm of Hg}$  (Fig S3b). This is comparable to the pressures found on the ocean seabed, under several kilometers of water ( $2.0 \times 10^5 \text{ mm of Hg} = 2.7 \text{ km of water}$ ), which is physically implausible. Our model does not consider the asymmetric time course of the heartbeat pulsation waveform, the non-circular shape of the PVS or the PVS surrounding pial arterioles<sup>16,17</sup>. We addressed these questions in a different study<sup>81</sup>, where we showed that unphysiologically large amplitude pulsations (with a peak-to-peak diameter change of 50%) are required for appreciable pumping. Altering the PVS shape or waveform of the pulsation did not achieve directional pumping. Instead, these simulations<sup>81</sup> showed that directional CSF flow, as observed in experiments<sup>16,17</sup>, can be explained by very small ( $<0.05 \text{ mm Hg}$ ) pressure differences in the system that could be naturally<sup>82</sup> occurring, or generated by the injections of a tracer<sup>83,84</sup>.

Modeling the brain-PVS interface as fixed in position presumes that the brain tissue is non-compliant. This assumption is only valid if the pressures produced are small relative to the elastic modulus of the brain. When the brain is presumed non-compliant, our simulations show that the peak pressures in the PVS during pulsations can reach 11 mmHg (Fig 2c) ( $0.32 \text{ mm Hg}$  for Navier-Stokes). Given that the brain is a soft tissue

with a shear modulus in the range of 1-8 kPa<sup>29-32</sup> (7-30 mmHg), we estimated that the peak displacement of the brain tissue induced by the pressure profile in Fig 2c would be 3.59  $\mu\text{m}$  (with a shear modulus of 4 kPa). The pressure profile for the Navier-Stokes model (Fig S2b) predicts a displacement of 0.08  $\mu\text{m}$ . This displacement cannot be ignored, because the arteriolar wall displacement driving the flow is only 0.06  $\mu\text{m}$ . We conclude that pressures induced by the flow demand that the mechanical properties of brain tissue and its deformability must be accounted for to accurately simulate fluid dynamics.

### **Arteriolar pulsations do not drive fluid exchange in a compliant brain model**

We modified our model by treating the brain as a compliant, elastic solid (Fig 3a). The pressure and the fluid shear forces in the PVS were coupled to the elastic deformation in the brain tissue using force-balance equations at the interface. We coupled the fluid velocity with the velocity of deforming brain tissue, to create a fully-coupled, fluid-structure interaction model (Fig 3b). In this model, the pressure changes in the PVS directly affect the deformation of the brain tissue and have a feedback effect on the flow in the PVS. The balance laws and boundary conditions used in this problem are described in methods.

We investigated how a compliant brain tissue model would respond to arteriolar pulsations. We imposed movement of the arteriolar wall with the same dynamics used in our previous model and visualized the resulting fluid flow in the axial direction ( $v_z$ ) (Fig 3c). Throughout the pulsation cycle, most of the fluid in the PVS showed little to no movement (white). Arteriolar pulsations driven by heartbeat cause a mere 0.21% ( $Q_f = 0.0021$ ) of the fluid in the PVS to be exchanged with the SAS and the parenchyma per cardiac cycle.

This lack of movement of fluid in the PVS in response to arteriolar pulsations held true over a wide range of changes in assumptions and parameters. Changing the brain tissue model from nearly incompressible (Poisson's ratio of 0.45) to a completely incompressible (Poisson's ratio of 0.5), Neo-Hookean model (Fig S4) had minimal impact on the pulsation-induced flow. Pulsation-driven flows were also small in simulations where the subarachnoid space (SAS) was modeled as a fluid-filled region connected to the PVS (Fig S5). We also studied flow driven by pulsations with different values of PVS width, permeability and shear modulus of the brain tissue (Fig S9). Even when the fluid flow is modeled using the Navier-Stokes equations (the infinite permeability case in Fig S9c), only 1.37% of the fluid in the PVS was exchanged with the SAS and the parenchyma, indicating that heart-beat pulsations cannot improve the transport of metabolites between the PVS and the SAS. These small flows were due to the compliance of the brain, as any pressure gradient that could generate substantial fluid movement will be dissipated on deforming the brain tissue instead. This result is in contrast to the calculations of Asgari *et al.*<sup>13</sup>, which suggested that the pulsatile flow in the PVS could improve metabolite clearance through dispersion. The relatively large pulsatile velocities calculated by Asgari *et al.*<sup>13</sup>, in the range of 120 $\mu\text{m/s}$  (as opposed to our calculations of less than 25 $\mu\text{m/s}$ ) can be attributed to not considering the elastic response of the brain tissue.

The flow observed in these simulations has a Reynolds number of  $1.14 \times 10^{-4}$ . The average downstream velocity of fluid was  $2.6 \times 10^{-3} \mu\text{m/s}$ . To understand the flow near the brain surface and into the PVS, we define two Péclet numbers,  $Pe_0$  and  $Pe_{50}$ , near the surface of the brain ( $z=La$ ) and 50 $\mu\text{m}$  below the surface ( $z=La - 50\mu\text{m}$ ) of the brain respectively (see methods). For these simulations, the values of  $Pe_0$  and  $Pe_{50}$  are

0.82 and 0.19 respectively, confirming that transport in the PVS away from the surface of the brain appears to be diffusion-dominated.

### **Arteriolar dilations during functional hyperemia can drive fluid exchange in the PVS**

While cardiac pulsations are small in size, the arteriolar dilations that accompany increases in local neural activity are substantially larger and longer lasting. In contrast with arteriolar pulsations which occur at the heart rate, these neurally-induced arteriolar dilations take one to three seconds to peak and last for several seconds in response to a brief increase in neural activity. In response to increases in local neural activity, cerebral arterioles can dilate by 20% or more in non-anesthetized animals<sup>85–88</sup>. These dilations induce blood flow changes that are the basis for the blood-oxygen-level dependent (BOLD), functional magnetic resonance imaging (fMRI)<sup>89–92</sup> signal.

To study the fluid exchange in the PVS driven by functional hyperemia, we imposed arteriolar wall motion in our model that matched those observed in awake mice during a typical functional hyperemic event<sup>41,42,79</sup> (Fig 4a). The mathematical formulation of this problem is identical to the previous simulation, with the exception that the arteriolar wall movement was given by a typical vasodilation profile instead of a heartbeat-driven peristaltic wave (Fig 4a). Compared to the flow driven by arteriolar pulsations, functional hyperemia-driven flow in the PVS had substantially higher flow velocities (Fig 4a). The fluid movement in these simulations was substantial and indicated that arteriolar dilations due to a single brief hyperemic event could exchange nearly half ( $Q_f = 0.4946$ ) of the fluid in the PVS with the SAS. The simulations also suggest that the pressure changes in the PVS due to this flow will deform the brain tissue by up to 1.2  $\mu\text{m}$  for an arteriolar dilation of 1.8  $\mu\text{m}$  (Fig S6). To check the robustness of these results, we repeated this simulation with a wide range of parameters (Fig S9), as well as with a Neo-Hookean (incompressible elastic) model (Fig S7). We also modeled the SAS as a fluid filled region connected to the PVS (Fig S8). In all cases, functional hyperemia-like dilations drove substantial fluid movement in the PVS. Compared to arteriolar pulsations, the vasodilation driven fluid exchange between PVS and SAS was two orders of magnitude higher under a wide range of model parameters (Fig S9). When the fluid is modeled by the Navier-Stokes equations (infinite permeability in Fig S9c), 69.8% of fluid in the PVS is exchanged with the SAS.

Because the fluid movement from arteriolar pulsations and functional hyperemia occur at different time scales (nominally 10 Hz and 0.2 Hz, respectively), we directly compared the fluid movement driven by arteriolar pulsations and functional hyperemia over equal time periods. This was achieved by calculating fluid particle trajectories in the deforming geometry of the PVS (see appendix for full mathematical description of boundary value problem for particle tracking in a deforming domain). The blue-green dots in Fig 4b represent fluid in the PVS, with the colormap showing the initial position (depth) of the fluid particle in the PVS. Fluid particles near the SAS (red dots) are added once every 0.5 secs to the calculation to simulate the possibility of fluid exchange between the PVS and the SAS. The results of these calculations indicate that a single hyperemic event can cause substantially more fluid movement in the PVS compared to arteriolar pulsations over the same time (Fig 4b, also see videos SV1 and SV2). These calculations suggest that when the flow in the PVS is modeled with coupled soft brain tissue mechanics, functional hyperemia can drive appreciable fluid exchange between the PVS and the SAS, while arteriolar pulsations do not drive

flow. The flow observed in these simulations has a Reynolds number of  $4.15 \times 10^{-4}$ . The average downstream velocity of fluid (over 10s) was  $0.12 \mu\text{m/s}$ . The values of  $Pe_0$  and  $Pe_{50}$  for these simulations are 2.97 and 1.96 respectively, showing that the fluid exchange caused by vasodilation can improve metabolite clearance compared to diffusion.

There are two main reasons why functional hyperemia drives large fluid exchange between the PVS and the SAS, while arteriolar pulsations are ineffective at driving fluid movement in the PVS. Firstly, heartbeat-driven changes in arteriolar diameter are very small ( $0.5\text{-}4\%^{16}$ ) in magnitude compared to neural activity-driven vasodilation ( $10\text{-}40\%^{42}$ ) and therefore there is a large difference in the volume of fluid displaced by the two mechanisms. Our measurements *in-vivo* also confirmed that the diameter changes driven by heartbeat (Fig S10) are in the  $0.5\text{-}4\%$  range while the diameter changes driven by vasodilation are in the  $10\text{-}40\%$  range (Fig 5m). A difference in the magnitude of blood volume change driven by heartbeat and hyperemia has also been observed in macaques<sup>93</sup> and humans<sup>94</sup> using functional magnetic resonance imaging (fMRI). Secondly, there is a large difference in the frequency of pulsations ( $7\text{-}14 \text{ Hz}^{57}$  in mice, nominally  $1 \text{ Hz}$  in humans) and hyperemic ( $0.1\text{-}0.3 \text{ Hz}^{79,95}$ ) motions of arteriolar walls. Fast (high frequency) movement of arteriolar walls cause larger changes in pressure, which will deform the brain tissue rather than driving fluid flow. Also, deformable (elastic) elements absorb more energy at higher frequencies. If the electrical circuit equivalent of flow through the PVS while ignoring brain deformation is analogous to a resistor, the equivalent of flow through the PVS with a deformable brain is analogous to a resistor and inductor in series (Fig S11a-b). In other words, arteriolar wall motion at higher frequencies drives less fluid movement compared to arteriolar wall movement at lower frequencies. A similar phenomenon has been studied extensively in the context of blood flow through deformable arteries and veins<sup>96-99</sup>. We compared the fluid exchange percentage for an arteriolar wall movement given by a sine wave ( $4\%$  peak to peak) of different frequencies, and found that the fluid exchange percentage has an inverse power law relation to frequency ( $f$ ) ( for the default parameters, Fig S11c).

### **In-vivo brain tissue deformation is consistent with a fluid-structure interaction model**

One of the main predictions of the fluid-structure interaction model is the deformation of the soft brain tissue in response to the pressure changes in the PVS driven by arteriolar dilation. To test this prediction, we measured displacement of the cortical brain tissue surrounding penetrating arterioles in awake, head-fixed B6.Cg-Tg(Thy1-YFP)16Jrs/J (Jackson Laboratory) mice<sup>100</sup> using two-photon laser scanning microscopy<sup>41</sup>. These transgenic mice express the fluorescent protein YFP in a sparse subset of pyramidal neurons whose axons and dendrites are strongly fluorescent<sup>101</sup>. Mice were implanted with polished, reinforced thinned-skull windows<sup>40</sup>(Fig 5a) to avoid inflammation<sup>102</sup>, disruption of mechanical properties<sup>103</sup> and the hemodynamic and metabolic effects<sup>104</sup> associated with craniotomies. We simultaneously imaged processes of Thy1-expressing neurons and blood vessel diameters (labeled via intravenous injection of Texas-red dextran) (Fig 5b). Arterioles in the somatosensory cortex dilate during spontaneous locomotion events due to increases in local neural activity<sup>79</sup>, so we imaged these vessels that will be naturally subject to large vasodilation. We performed piecewise, iterative motion correction of the collected images relative to the center of the arteriole

(see Methods) in order to robustly measure the displacement of brain tissue during arteriolar dilations. We visually verified the measured brain tissue displacements.

We considered two possible paradigms of brain deformation, a “non-compliant brain” model and a fluid-structure interaction model. We predict the two paradigms to yield completely different results in terms of the displacement of the brain tissue observed in-vivo. In the non-compliant brain model, the brain tissue will be unaffected by pressure changes in the PVS. In this model, pulsations and small dilations of arterioles would cause flow in the PVS but no displacement of the brain tissue (Fig 5c). Only after the arteriolar wall comes in contact with the brain tissue (and the PVS has fully collapsed), arteriolar dilation would cause tissue displacement (Fig 5d). Therefore, displacement in the brain tissue in this model would be either non-existent (for small dilations), or similar to a “trimmed” version of the displacement of the arteriolar wall (Fig 5e). Alternatively, in the fluid-structure interaction model, any movement of the arteriolar wall that can drive fluid flow in the PVS will result in pressure changes in the PVS that are sufficient to deform the ‘soft’ brain tissue, as predicted by our simulations (Fig 5f, 5g). Therefore, displacement should be observed in the brain tissue as soon as the arteriolar wall starts to dilate. In the fluid-structure interaction model, the radial displacement in the brain tissue would be a scaled version of the radial displacement of the arteriolar wall (Fig 5h).

We calculated the radial displacement of the arteriolar wall and the brain tissue in-vivo ( $n = 21$  vessels, 7 mice) using two-photon microscopy. The radial displacement of the brain tissue was between 20-80% of the radial displacement of the arteriolar wall. The simulations suggest that such a variation is to be expected due to heterogeneity in the width and depth of the PVS and variations in the distance of the plane of imaging from the surface of the brain (Fig S6a and S6b). Despite the variation in the amplitude of displacement in the tissue, our simulations predict that the waveform of the displacement in the tissue should be very consistent. In particular the peak-normalized displacement response of the brain tissue should almost identical everywhere (Fig S6c). We used this result from the simulation to test the predictions of the model experimentally. We calculated the peak normalized impulse response of the displacements to locomotion (Fig 5n). The calculations of tissue displacement for each arteriole (an example is shown in Fig 5j-m), as well as the normalized impulse response for the brain tissue (Fig 5n) suggest that the displacement in the brain tissue started as soon as the arteriolar dilations started. This implies that the brain tissue can deform due to pressure changes in the PVS, as predicted by the fluid-structure interaction model. Note that all the displacement values in the brain tissue used for calculating the average waveform reported in Fig 5n were subject to a rigorous set of tests (see Methods) to account for motion artifacts. To visualize the brain tissue displacements accompanying vasodilation, we plotted a kymogram taken along diameter line bisecting the arteriole and crossing neural processes (Fig 5k, 5l). Distance from the center of the arteriole is on the x-axis and time on the y-axis. Dilations appear as a widening of the vessel, while displacements of the brain tissue will show up as shifts on the x axis. This visualization was used as an additional step in validating the displacement values calculated by our method. For calculating the average waveform of tissue displacement shown in Fig 5n, only one of the calculated displacement values per vessel that could also be visually verified was used. The displacement of the brain tissue is also apparent from visualizing the data. Supplementary video SV3 shows 50 seconds of imaging data, where we can observe the brain tissue (green) deforms in response to dilation of the vessel (magenta).

Interestingly, the fluid-structure interaction model predicted a negative radial displacement in the brain tissue, when the arteriole constricts or returns to its original diameter, which we did not observe. This anomaly can be explained by the fact that the fluid-structure interaction model neglects the elastic forces in the connective tissue (extracellular matrix) in the PVS. The PVS contains collagen fibers and fibroblasts, that are continuous with the extracellular space of the surrounding tissue<sup>105,106</sup>. Collagen networks can have a highly non-linear elastic response when the loading is changed from compression to tension, and exhibit hysteresis during large, cyclic deformations<sup>107,108</sup>. The elastic modulus of fibrous networks under tension can be 2-3 orders of magnitude higher than the elastic modulus in compression<sup>109-111</sup>. Connective tissue is made up of networks of fibers and the energy cost of bending these fibers is several orders of magnitude smaller than stretching them. When the arteriole dilates, these fibers are subject to a compressive loading and they buckle (bend) rather than compress, and as a result generate very little elastic forces (Fig S12b). On the other hand, when the arteriole constricts or returns to its initial size, these fibers are subjected to a tensile load (Fig S12c) and produce significantly higher (2-3 orders of magnitude higher) elastic forces. However, our model only considers the fluid-dynamic forces in the PVS and neglects the elastic forces. This is one of the shortcomings of our model, that can be corrected in the future using models of poroelasticity<sup>112-114</sup> so as to account for the mutual interaction of flow and deformation within the PVS. Alternatively, the predicted negative radial displacement might be an artifact of modelling the brain tissue with a Poisson's ratio of 0.45-0.5. While this range of Poisson's ratio might be adequate to simulate the elastic behavior of the brain under compression, the brain behaves like a solid with a Poisson's ratio of 0.3 under tension<sup>74</sup>.

## Discussion

A summary of the model parameters and main results of all the simulations in this article are shown in Table 2 below. The pressure changes observed in the PVS, while assuming the brain tissue as non-compliant can cause appreciable deformation in the brain. For all the fluid-structure interaction models, the percentage of PVS fluid exchanged with the SAS is the main metric for metabolite clearance. The mean downstream speed (net directional flow velocity into the parenchyma) is negligible for all cases with realistic length of the arteriole.

### **Table 2: Summary of Simulations**

Figure	Brain model	Fluid Permeability (m <sup>2</sup> )	Arteriolar wall movement	Mean downstream speed (μm/s)	PVS fluid exchanged with SAS	Conclusion
2	Non-compliant	2x10 <sup>-14</sup>	Heartbeat ΔR <sub>max</sub> = 0.06 μm	5.5 x 10 <sup>-4</sup>	-	Expected brain deformation, 3.59 μm > pulsation amplitude, 0.06 μm
3	SVK, μ <sub>s</sub> = 4kPa (compressible)	2x10 <sup>-14</sup>	Heartbeat ΔR <sub>max</sub> = 0.06 μm	2.6 x 10 <sup>-3</sup>	0.21%	No appreciable fluid exchange
4	SVK, μ <sub>s</sub> = 4kPa (compressible)	2x10 <sup>-14</sup>	Hyperemia ΔR <sub>max</sub> = 1.8 μm	0.12	49.46%	Appreciable fluid exchange
S1	Non-compliant	∞ (Navier-Stokes)	Heartbeat ΔR <sub>max</sub> = 0.06 μm	1.8 x 10 <sup>-3</sup>	-	Expected brain deformation, 0.08 μm > pulsation amplitude, 0.06 μm
S2	Non-compliant	2x10 <sup>-14</sup> No SAS/parenchyma flow resistances	Heartbeat ΔR <sub>max</sub> = 0.06 μm	2.6 x 10 <sup>-3</sup>	-	Expected brain deformation, 0.71 μm > pulsation amplitude, 0.06 μm
S3	Non-compliant	2x10 <sup>-14</sup> Arteriole length = 100mm	Heartbeat ΔR <sub>max</sub> = 0.06 μm	143.2	-	Flow accompanied by 200,000 mmHg pressure changes
S4	Neo-Hookean, μ <sub>s</sub> = 4kPa (Incompressible)	2x10 <sup>-14</sup>	Heartbeat ΔR <sub>max</sub> = 0.06 μm	1.1 x 10 <sup>-4</sup>	0.18%	No appreciable fluid exchange
S5	SVK, μ <sub>s</sub> = 4kPa (compressible)	2x10 <sup>-14</sup> SAS geometry explicitly modeled	Heartbeat ΔR <sub>max</sub> = 0.06 μm	2.6 x 10 <sup>-3</sup>	0.23%	No appreciable fluid exchange
S6	SVK, μ <sub>s</sub> = 4kPa (compressible)	2x10 <sup>-14</sup>	Hyperemia ΔR <sub>max</sub> = 1.8 μm	0.12	49.46%	Tissue displacement has a typical waveform
S7	Neo-Hookean, μ <sub>s</sub> = 4kPa (Incompressible)	2x10 <sup>-14</sup>	Hyperemia ΔR <sub>max</sub> = 1.8 μm	0.13	50.92%	Appreciable fluid exchange
S8	SVK, μ <sub>s</sub> = 4kPa	2x10 <sup>-14</sup>	Hyperemia	0.12	49.66%	Appreciable

	(compressible)	SAS geometry explicitly modeled	$\Delta R_{\max} = 1.8 \mu\text{m}$			fluid exchange
S9a	SVK, $\mu_s = 1-8$ kPa	$2 \times 10^{-14}$	Heartbeat/Hyperemia $\Delta R_{\max} = 0.06/1.8 \mu\text{m}$	-	Heartbeat 0.09-0.29% Hyperemia 26.96 - 59.55%	Fluid exchange of hyperemia $\approx$ 200 x fluid exchange of heartbeat
S9b	SVK, $\mu_s = 4$ kPa	$2 \times 10^{-14}$ PVS width = 3-9 $\mu\text{m}$	Heartbeat/Hyperemia $\Delta R_{\max} = 0.06/1.8 \mu\text{m}$	-	Heartbeat 0.08-0.21% Hyperemia 17.88 - 49.46%	Fluid exchange of hyperemia $\approx$ 200 x fluid exchange of heartbeat
S9c	SVK, $\mu_s = 4$ kPa	$2 \times 10^{-15} - 7 \times 10^{-13}$ & $\infty$ (Navier-Stokes)	Heartbeat/Hyperemia $\Delta R_{\max} = 0.06/1.8 \mu\text{m}$	-	Heartbeat 0.06-1.37% Hyperemia 17.85 - 70.55%	Fluid exchange of hyperemia $\approx$ 200 x fluid exchange of heartbeat
S11	SVK, $\mu_s = 4$ kPa	$2 \times 10^{-14}$	$\Delta R_{\max} = 0.24 \mu\text{m}$ Frequency, $f = 0.05-10\text{Hz}$	-		Fluid exchange is inversely related to frequency of arteriolar wall movement

While there have been several models investigating the fluid mechanics in the PVS<sup>13,19,28</sup>, to our knowledge, none of them considered the impact of the soft, deformable brain tissue on CSF flow in the PVS. Our simulations show that fluid flow in a porous PVS resulting from the movement of the vessel walls can be affected by the deformability of the brain tissue. We have also presented empirical evidence to support our claim that the brain tissue deforms in response to pressure changes in the PVS. As far as we know, this is the first study to include deformability of the brain tissue in modeling fluid flow in the PVS and to use experiments to support the predictions of fluid dynamic simulations.

Our model has some limitations and the results should be interpreted with these limitations in mind. We assumed a cylindrically symmetric geometry for our model. In reality, the PVS around penetrating vessels can be eccentric and elliptical<sup>16</sup>. An eccentric annular region with a pulsating inner wall can cause a slow drift in the fluid particles<sup>115</sup> (however, the drift caused by eccentricity is not unidirectional, and the bulk movement of the particles is much smaller compared to the oscillations<sup>16,17</sup>). We neglected the possibility of fluid flow within the brain parenchyma and the effect of the aquaporin-4 channels found on the astrocyte endfeet lining the brain-PVS interface<sup>10</sup>. We have avoided simulating this route of fluid flow mainly because of the controversy regarding bulk flow through the parenchyma. This can be rectified in future studies by using models of poroelasticity<sup>112-114</sup>, which simultaneously simulate fluid movement through the

extracellular space and the deformations in the brain tissue. Some authors have used poroelastic models to predict that oscillatory flows can enhance metabolite transport in the brain through dispersion<sup>116</sup>. Poroelastic models can also explore the effect of static and dynamic occlusions to flow<sup>117,118</sup>, which our fluid-structure model does not simulate. We also ignore the elastic response of the collagen fibers in the PVS and simulate and only simulate the fluid dynamics in this region.

Our results are in agreement with the findings of several experimental studies<sup>16,17,21,38,119,120</sup>, though they cast their results in a new light. Several studies have used microspheres to visualize the CSF movement in the PVS around pial arterioles<sup>16,17</sup>. Similar to their results, our simulations suggest that CSF oscillates with the frequency of heartbeat driven pulsations near the surface of the brain (Fig 3c, Figures S3 and S4). It can also be shown that larger arteriolar pulsations can cause larger oscillations in CSF flow, similar to the case of induced hypertension found by Mestre *et al*<sup>16</sup>. In contrast to the conclusions of these particle tracking studies<sup>16,17</sup>, our simulations suggest that arteriolar pulsations do not provide a driving force for net unidirectional movement of CSF. This lack of unidirectional flow is consistent with molecular weight-dependent transport of dyes observed with intra-parenchymal tracer injection in mice<sup>21</sup> and intrathecal injections in rats<sup>38,121</sup>. Our results also agree with the findings that voluntary running, which increases neural activity<sup>122,123</sup> and induces functional hyperemia<sup>95,124</sup> in several regions of the brain, enhances penetration of tracers in the brain parenchyma, when injected into the cisterna magna<sup>119</sup>. The silencing of neural activity<sup>125,126</sup> (and therefore vascular activity) by anesthetics<sup>127,128</sup> could explain diminished penetration of tracers in the brain parenchyma, when injected into the cisterna magna under anesthesia<sup>129</sup>. The variability in results between groups may be influenced by anesthesia type and levels, both of which have large effects on the amplitude of the arteriolar dilations elicited during functional hyperemia<sup>42</sup>. Finally, brain-wide hyperemia observed during REM sleep<sup>130</sup> could explain improved tracer transport in the brain observed during sleep<sup>120</sup>. We do not claim that functional hyperemia improves flow in the proposed “glymphatic” pathway<sup>131</sup>, as we did not model flow through the brain extracellular space or the paravenous space.

Our results have implications for the development and treatment of CNS disorders and suggest that in addition to its other physiological roles, functional hyperemia may serve to improve transport into and out of the brain by driving exchange of fluid in the PVS with the SAS. Many studies support the idea that vascular dysfunction can be a precursor to neurodegenerative diseases<sup>132–134</sup>. Our simulations suggest a mechanistic relation between neurovascular coupling and metabolite clearance from the brain, which could explain the development of neurodegenerative diseases like Alzheimer’s. The response of our model to changes in key parameters can explain the effect of aging on clearance of metabolic waste from the brain. Some studies have shown that the elastic modulus of the brain decreases with aging<sup>54,55</sup>, and our model predicts less fluid exchange between the SAS and the PVS when the elastic modulus is lowered (Fig S9a). Finally, the increase of PVS width observed with aging<sup>135</sup> might be a reason for reduced clearance of metabolic waste from the brain (Fig S9b). While these possibilities are admittedly speculative, they may be fertile ground for further investigation of the interaction of brain mechanics and health.

## Methods

Due to technical limitations, the Methods section is only available as a download in the supplemental files section

## Declarations

### Availability of data and materials

All the data and simulation files are available on Box (<https://psu.box.com/s/xrcs2ojzs4gg0w6q2aokv5zggoybndcfw>).

### Ethics

All procedures were performed in accordance with protocols approved by the Institutional Animal Care and Use Committee (IACUC) of Pennsylvania State University.

### Author Contributions

P.J.D., B.J.G. and F.C. were responsible for conceptualization and are the principal investigators on the grant. K.L.T. and C.E. performed surgeries on animals and were responsible for animal care. R.K. was responsible for the simulations, data acquisition and analysis. The simulations were supervised by F.C. The data acquisition and analysis were supervised by P.J.D. R.K. drafted the initial manuscript. All the authors reviewed the manuscript.

### Competing interests

The authors declare that they have no competing interests.

## References

1. Cserr, H. F., Harling-Berg, C. J. & Knopf, P. M. Drainage of Brain Extracellular Fluid into Blood and Deep Cervical Lymph and its Immunological Significance. *Brain Pathol.* **2**, 269–276 (1992).
2. Bradbury, M. W. B., Cserr, H. F. & Westrop, R. J. Drainage of cerebral interstitial fluid into deep cervical lymph of the rabbit. *Am. J. Physiol. - Ren. Fluid Electrolyte Physiol.* **9**, 329–336 (1981).
3. Louveau, A., Da Mesquita, S. & Kipnis, J. Lymphatics in Neurological Disorders: A Neuro-Lympho-Vascular Component of Multiple Sclerosis and Alzheimer's Disease? *Neuron* **91**, 957–973 (2016).
4. Louveau, A. *et al.* Structural and functional features of central nervous system lymphatic vessels. *Nature* **523**, 337–341 (2015).
5. Aspelund, A. *et al.* A dural lymphatic vascular system that drains brain interstitial fluid and macromolecules. *J. Exp. Med.* **212**, 991–999 (2015).
6. Weller, R. O., Kida, S. & Zhang, E. -T. Pathways of Fluid Drainage from the Brain - Morphological Aspects and Immunological Significance in Rat and Man. *Brain Pathol.* **2**, 277–284 (1992).
7. Qiuhan, Z. *et al.* Lymphatic Drainage of the Skull Base: Comparative Anatomic and Advanced Imaging Studies in the Rabbit and Human With Implications for Spread of Nasopharyngeal Carcinoma.

- Lymphology* **43**, 98–109 (2010).
8. Smith, A. J. & Verkman, A. S. CrossTalk opposing view: Going against the flow: interstitial solute transport in brain is diffusive and aquaporin-4 independent. *J. Physiol.* **0**, 1–4 (2019).
  9. Iiff, J. & Simon, M. CrossTalk proposal: The glymphatic system supports convective exchange of cerebrospinal fluid and brain interstitial fluid that is mediated by perivascular aquaporin-4. *J. Physiol.* **0**, 1–3 (2019).
  10. Abbott, N. J., Pizzo, M. E., Preston, J. E., Janigro, D. & Thorne, R. G. The role of brain barriers in fluid movement in the CNS: is there a 'glymphatic' system? *Acta Neuropathol.* **135**, 1–21 (2018).
  11. Smith, A. J., Yao, X., Dix, J. A., Jin, B. J. & Verkman, A. S. Test of the 'glymphatic' hypothesis demonstrates diffusive and aquaporin-4-independent solute transport in rodent brain parenchyma. *Elife* **6**, 1–16 (2017).
  12. Jin, B.-J., Smith, A. J. & Verkman, A. S. Spatial model of convective solute transport in brain extracellular space does not support a "glymphatic" mechanism. *J. Gen. Physiol.* **148**, 489–501 (2016).
  13. Asgari, M., De Zélicourt, D. & Kurtcuoglu, V. Glymphatic solute transport does not require bulk flow. *Sci. Rep.* **6**, 1–11 (2016).
  14. Holter, K. E. *et al.* Interstitial solute transport in 3D reconstructed neuropil occurs by diffusion rather than bulk flow. *Proc. Natl. Acad. Sci.* 201706942 (2017). doi:10.1073/pnas.1706942114
  15. Iiff, J. J. *et al.* Cerebral Arterial Pulsation Drives Paravascular CSF-Interstitial Fluid Exchange in the Murine Brain. *J. Neurosci.* **33**, 18190–18199 (2013).
  16. Mestre, H. *et al.* Flow of cerebrospinal fluid is driven by arterial pulsations and is reduced in hypertension. *Nat. Commun.* **9**, 4878 (2018).
  17. Bedussi, B., Almasian, M., de Vos, J., VanBavel, E. & Bakker, E. N. Paravascular spaces at the brain surface: Low resistance pathways for cerebrospinal fluid flow. *J. Cereb. Blood Flow Metab.* 0271678X1773798 (2017). doi:10.1177/0271678X17737984
  18. Iiff, J. J. *et al.* Cerebral Arterial Pulsation Drives Paravascular CSF – Interstitial Fluid Exchange in the Murine Brain. **33**, 18190–18199 (2013).
  19. Wang, P. & Olbricht, W. L. Fluid mechanics in the perivascular space. *J. Theor. Biol.* **274**, 52–57 (2011).
  20. Thomas, J. H. Fluid dynamics of cerebrospinal fluid flow in perivascular spaces. *J. R. Soc. Interface* **16**, (2019).
  21. Smith, A. J., Yao, X., Dix, J. A., Jin, B. & Verkman, A. S. Test of the 'glymphatic' hypothesis demonstrates diffusive and aquaporin-4-independent solute transport in rodent brain parenchyma. 1–16 (2017). doi:10.7554/eLife.27679
  22. Binder, D. K., Papadopoulos, M. C., Haggie, P. M. & Verkman, A. S. In vivo measurement of brain extracellular space diffusion by cortical surface photobleaching. *J. Neurosci.* **24**, 8049–8056 (2004).
  23. Norwood, J. N. *et al.* Anatomical basis and physiological role of cerebrospinal fluid transport through the murine cribriform plate. *Elife* **8**, 1–32 (2019).
  24. Coles, J. A., Myburgh, E., Brewer, J. M. & McMenamin, P. G. Where are we? The anatomy of the murine cortical meninges revisited for intravital imaging, immunology, and clearance of waste from the brain.

- Prog. Neurobiol.* **156**, 107–148 (2017).
25. Damkier, H. H., Brown, P. D. & Praetorius, J. Cerebrospinal fluid secretion by the choroid plexus. *Physiol. Rev.* **93**, 1847–1892 (2013).
  26. Sweetman, B. & Linninger, A. A. Cerebrospinal fluid flow dynamics in the central nervous system. *Ann. Biomed. Eng.* **39**, 484–496 (2011).
  27. Dreha-Kulaczewski, S. *et al.* Inspiration is the major regulator of human CSF flow. *J. Neurosci.* **35**, 2485–2491 (2015).
  28. Schley, D., Carare-Nnadi, R., Please, C. P., Perry, V. H. & Weller, R. O. Mechanisms to explain the reverse perivascular transport of solutes out of the brain. *J. Theor. Biol.* **238**, 962–974 (2006).
  29. Goriely, A. *et al.* Mechanics of the brain: perspectives, challenges, and opportunities. *Biomech. Model. Mechanobiol.* **14**, 931–965 (2015).
  30. Weickenmeier, J. *et al.* Brain stiffens post mortem. *J. Mech. Behav. Biomed. Mater.* **84**, 88–98 (2018).
  31. Mihai, L. A., Budday, S., Holzapfel, G. A., Kuhl, E. & Goriely, A. A family of hyperelastic models for human brain tissue. *J. Mech. Phys. Solids* **106**, 60–79 (2017).
  32. Budday, S. *et al.* Mechanical characterization of human brain tissue. *Acta Biomater.* **48**, 319–340 (2017).
  33. Sweetman, B., Xenos, M., Zitella, L. & Linninger, A. A. Three-dimensional computational prediction of cerebrospinal fluid flow in the human brain. *Comput. Biol. Med.* **41**, 67–75 (2011).
  34. Miller, K. & Kurtcuoglu, V. Biomechanics of the Brain. *Biomech. Brain* 169–188 (2011). doi:10.1007/978-1-4419-9997-9
  35. Gupta, S. *et al.* Cerebrospinal fluid dynamics in the human cranial subarachnoid space: An overlooked mediator of cerebral disease. I. Computational model. *J. R. Soc. Interface* **7**, 1195–1204 (2010).
  36. Linninger, A. A. *et al.* Cerebrospinal fluid flow in the normal and hydrocephalic human brain. *IEEE Trans. Biomed. Eng.* **54**, 291–302 (2007).
  37. Fin, L. & Grebe, R. Three dimensional modeling of the cerebrospinal fluid dynamics and brain interactions in the aqueduct of sylvius. *Comput. Methods Biomech. Biomed. Engin.* **6**, 163–170 (2003).
  38. Pizzo, M. E. *et al.* Intrathecal antibody distribution in the rat brain: surface diffusion, perivascular transport and osmotic enhancement of delivery. *J. Physiol.* **596**, 445–475 (2018).
  39. Martinac, A. D. & Bilston, L. E. Computational modelling of fluid and solute transport in the brain. *Biomech. Model. Mechanobiol.* (2019). doi:10.1007/s10237-019-01253-y
  40. Drew, P. J. *et al.* Chronic optical access through a polished and reinforced thinned skull. *Nat. Methods* **7**, 981–984 (2010).
  41. Shih, A. Y. *et al.* Two-photon microscopy as a tool to study blood flow and neurovascular coupling in the rodent brain. *J. Cereb. Blood Flow Metab.* **32**, 1277–1309 (2012).
  42. Gao, Y. R. *et al.* Time to wake up: Studying neurovascular coupling and brain-wide circuit function in the un-anesthetized animal. *Neuroimage* **153**, 382–398 (2017).
  43. Horton, N. G. *et al.* In vivo three-photon microscopy of subcortical structures within an intact mouse brain. *Nat. Photonics* **7**, 205–209 (2013).

44. Schain, A. J., Melo, A., Strassman, A. M. & Burstein, R. Cortical spreading depression closes the paravascular space and impairs glymphatic flow: Implications for migraine headache. *J. Neurosci.* **37**, 3390–16 (2017).
45. Iliff, J. J. *et al.* A Paravascular Pathway Facilitates CSF Flow Through the Brain Parenchyma and the Clearance of Interstitial Solutes, Including Amyloid. *Sci. Transl. Med.* **4**, 147ra111-147ra111 (2012).
46. Støverud, K. H., Langtangen, H. P., Haughton, V. & Mardal, K. A. CSF pressure and velocity in obstructions of the subarachnoid spaces. *Neuroradiol. J.* **26**, 218–226 (2013).
47. Yetkin, F. *et al.* Cerebrospinal fluid viscosity: a novel diagnostic measure for acute meningitis. *South Med J* **103**, 892–895 (2010).
48. Vanlandewijck, M. *et al.* A molecular atlas of cell types and zonation in the brain vasculature. *Nature* **554**, 475–480 (2018).
49. Neeves, K. B., Lo, C. T., Foley, C. P., Saltzman, W. M. & Olbricht, W. L. Fabrication and characterization of microfluidic probes for convection enhanced drug delivery. *J. Control. Release* **111**, 252–262 (2006).
50. Smith, J. H. & Humphrey, J. A. C. Interstitial transport and transvascular fluid exchange during infusion into brain and tumor tissue. *Microvasc. Res.* **73**, 58–73 (2007).
51. Adams, M. D., Winder, A. T., Blinder, P. & Drew, P. J. The pial vasculature of the mouse develops according to a sensory-independent program. *Sci. Rep.* **8**, 1–12 (2018).
52. Franceschini, G., Bigoni, D., Regitnig, P. & Holzapfel, G. A. Brain tissue deforms similarly to filled elastomers and follows consolidation theory. *J. Mech. Phys. Solids* **54**, 2592–2620 (2006).
53. Streitberger, K. J. *et al.* In vivo viscoelastic properties of the brain in normal pressure hydrocephalus. *NMR Biomed.* **24**, 385–392 (2011).
54. Sack, I., Streitberger, K. J., Krefting, D., Paul, F. & Braun, J. The influence of physiological aging and atrophy on brain viscoelastic properties in humans. *PLoS One* **6**, (2011).
55. Sack, I. *et al.* The impact of aging and gender on brain viscoelasticity. *Neuroimage* **46**, 652–657 (2009).
56. Barber, T. W., Brockway, J. A. & Higgins, L. S. The density of tissues in and about the head. *Acta Neurol. Scand.* **46**, 85–92 (1970).
57. Winder, A. T., Echagarruga, C., Zhang, Q. & Drew, P. J. Weak correlations between hemodynamic signals and ongoing neural activity during the resting state. *Nat. Neurosci.* **20**, 1761–1769 (2017).
58. Brands, P. J., Willigers, J. M., Ledoux, L. A. F. F., Reneman, R. S. & Hoeks, A. P. G. G. A noninvasive method to estimate pulse wave velocity in arteries locally by means of ultrasound. *Ultrasound Med. Biol.* **24**, 1325–1335 (1998).
59. Sarah GLADDISH & Chakravarthi RAJKUMAR. Repeatability of non-invasive measurement of intracerebral pulse wave velocity using transcranial Doppler. *Crit. Care Med.* **30**, 563–569 (2002).
60. Greenshields, C. J. & Weller, H. G. A unified formulation for continuum mechanics applied to fluid-structure interaction in flexible tubes. *Int. J. Numer. Methods Eng.* **64**, 1575–1593 (2005).
61. Massi, F., Peng, J. W., Lee, J. P. & Straub, J. E. Simulation study of the structure and dynamics of the Alzheimer's amyloid peptide congener in solution. *Biophys. J.* **80**, 31–44 (2001).

62. Tseng, B. P. *et al.* Deposition of monomeric, not oligomeric, A $\beta$  mediates growth of Alzheimer's disease amyloid plaques in human brain preparations. *Biochemistry* **38**, 10424–10431 (1999).
63. Brinkman, H. C. A calculation of the viscous force exerted by a flowing fluid on a dense swarm of particles. *Flow, Turbul. Combust.* **1**, 27 (1949).
64. Vafai, K. & Kim, S. J. On the limitations of the Brinkman-Forchheimer-extended Darcy equation. *Int. J. Heat Fluid Flow* **16**, 11–15 (1995).
65. Armstrong, J. K., Wenby, R. B., Meiselman, H. J. & Fisher, T. C. The hydrodynamic radii of macromolecules and their effect on red blood cell aggregation. *Biophys. J.* **87**, 4259–4270 (2004).
66. Bedussi, B. *et al.* Paravascular channels, cisterns, and the subarachnoid space in the rat brain: A single compartment with preferential pathways. *J. Cereb. Blood Flow Metab.* **37**, 1374–1385 (2017).
67. Potter, G. M. *et al.* Enlarged perivascular spaces and cerebral small vessel disease. *Int. J. Stroke* **10**, 376–381 (2015).
68. Potter, G. M., Chappell, F. M., Morris, Z. & Wardlaw, J. M. Cerebral Perivascular Spaces Visible on Magnetic Resonance Imaging: Development of a Qualitative Rating Scale and its Observer Reliability. **2015**, 224–231 (2015).
69. Albargothy, N. J. *et al.* Convective influx/glymphatic system: tracers injected into the CSF enter and leave the brain along separate periarterial basement membrane pathways. *Acta Neuropathol.* **136**, 139–152 (2018).
70. Weller, R. O., Sharp, M. M., Christodoulides, M., Carare, R. O. & Møllgård, K. The meninges as barriers and facilitators for the movement of fluid, cells and pathogens related to the rodent and human CNS. *Acta Neuropathol.* **135**, 363–385 (2018).
71. Korogod, N., Petersen, C. C. H. & Knott, G. W. Ultrastructural analysis of adult mouse neocortex comparing aldehyde perfusion with cryo fixation. *Elife* **4**, 1–17 (2015).
72. Kacem, K., Lacombe, P., Seylaz, J. & Bonvento, G. Structural organization of the perivascular astrocyte endfeet and their relationship with the endothelial glucose transporter: A confocal microscopy study. *Glia* **23**, 1–10 (1998).
73. Mestre, H. *et al.* Aquaporin-4-dependent glymphatic solute transport in the rodent brain. *Elife* **7**, 1–31 (2018).
74. Budday, S., Ovaert, T. C., Holzapfel, G. A., Steinmann, P. & Kuhl, E. *Fifty Shades of Brain: A Review on the Mechanical Testing and Modeling of Brain Tissue. Archives of Computational Methods in Engineering* (Springer Netherlands, 2019). doi:10.1007/s11831-019-09352-w
75. Leizea, I. *et al.* Real-time visual tracking of deformable objects in robot-assisted surgery. *IEEE Comput. Graph. Appl.* **37**, 56–68 (2015).
76. Wittek, A., Hawkins, T. & Miller, K. On the unimportance of constitutive models in computing brain deformation for image-guided surgery. *Biomech. Model. Mechanobiol.* **8**, 77–84 (2009).
77. Nishimura, N., Schaffer, C. B., Friedman, B., Lyden, P. D. & Kleinfeld, D. Penetrating arterioles are a bottleneck in the perfusion of neocortex. *Proc. Natl. Acad. Sci. U. S. A.* **104**, 365–370 (2007).
78. Blinder, P., Shih, A. Y., Rafie, C. & Kleinfeld, D. Topological basis for the robust distribution of blood to rodent neocortex. *Proc. Natl. Acad. Sci. U. S. A.* **107**, 12670–12675 (2010).

79. Gao, Y. R., Greene, S. E. & Drew, P. J. Mechanical restriction of intracortical vessel dilation by brain tissue sculpts the hemodynamic response. *Neuroimage* **115**, 162–176 (2015).
80. Bilston, L. E., Fletcher, D. F., Brodbelt, A. R. & Stoodley, M. A. Arterial pulsation-driven cerebrospinal fluid flow in the perivascular space: a computational model. *Comput. Methods Biomech. Biomed. Eng.* **6**, 235–241 (2003).
81. Kedarasetti, R., Drew, P. J. & Costanzo, F. Arterial pulsations drive oscillatory flow of CSF but not directional pumping. *bioRxiv* (2020).
82. Gao, X. Y. & Drew, P. J. Effects of Voluntary Locomotion and Calcitonin Gene-Related Peptide on the Dynamics of Single Dural Vessels in Awake Mice. **36**, 2503–2516 (2016).
83. Marmarou, A. & Shulman, K. Compartmental analysis of compliance and outflow resistance of the cerebrospinal fluid system. **di**, 523–534 (1975).
84. Marmarou, A., Shulman, K. & Rosende, R. M. A nonlinear analysis of the cerebrospinal fluid system and intracranial pressure dynamics. *J. Neurosurg.* **48**, 332–344 (1978).
85. Drew, P. J., Shih, A. Y. & Kleinfeld, D. Fluctuating and sensory-induced vasodynamics in rodent cortex extend arteriole capacity. *Proc. Natl. Acad. Sci.* **108**, 8473–8478 (2011).
86. Mishra, A. *et al.* Astrocytes mediate neurovascular signaling to capillary pericytes but not to arterioles. *Nat. Neurosci.* **19**, 1619 (2016).
87. Hill, R. A. *et al.* Regional blood flow in the normal and ischemic brain is controlled by arteriolar smooth muscle cell contractility and not by capillary pericytes. *Neuron* **87**, 95–110 (2015).
88. Rungta, R. L., Chaigneau, E., Osmani, B.-F. & Charpak, S. Vascular compartmentalization of functional hyperemia from the synapse to the pia. *Neuron* **99**, 362–375 (2018).
89. Goense, J. B. M. & Logothetis, N. K. Neurophysiology of the BOLD fMRI signal in awake monkeys. *Curr. Biol.* **18**, 631–640 (2008).
90. Hillman, E. M. C. Coupling mechanism and significance of the BOLD signal: a status report. *Annu. Rev. Neurosci.* **37**, 161–181 (2014).
91. Logothetis, N. K. What we can do and what we cannot do with fMRI. *Nature* **453**, 869 (2008).
92. Drew, P. J. Vascular and neural basis of the BOLD signal. *Curr. Opin. Neurobiol.* **58**, 61–69 (2019).
93. Teichert, T., Grinband, J., Hirsch, J. & Ferrera, V. P. Effects of heartbeat and respiration on macaque fMRI: Implications for functional connectivity. *Neuropsychologia* **48**, 1886–1894 (2010).
94. Dagli, M. S., Ingeholm, J. E. & Haxby, J. V. Localization of cardiac-induced signal change in fMRI. *Neuroimage* **9**, 407–415 (1999).
95. Huo, B. X., Gao, Y. R. & Drew, P. J. Quantitative separation of arterial and venous cerebral blood volume increases during voluntary locomotion. *Neuroimage* **105**, 369–379 (2015).
96. Rideout, V. C. & Dick, D. E. Difference-Differential Equations for Fluid Flow in Distensible Tubes. *IEEE Trans. Biomed. Eng.* **BME-14**, 171–177 (1967).
97. Müller, L. O. & Toro, E. F. Enhanced global mathematical model for studying cerebral venous blood flow. *J. Biomech.* **47**, 3361–3372 (2014).

98. Müller, L. O. & Toro, E. F. A global multiscale mathematical model for the human circulation with emphasis on the venous system. *Int. j. numer. method. biomed. eng.* **30**, 681–725 (2014).
99. Vignon-Clementel, I. E., Alberto Figueroa, C., Jansen, K. E. & Taylor, C. A. Outflow boundary conditions for three-dimensional finite element modeling of blood flow and pressure in arteries. *Comput. Methods Appl. Mech. Eng.* **195**, 3776–3796 (2006).
100. Feng, G. *et al.* Imaging neuronal subsets in transgenic mice expressing multiple spectral variants of GFP. *Neuron* **28**, 41–51 (2000).
101. Grutzendler, J., Kasthuri, N. & Gan, W.-B. Long-term dendritic spine stability in the adult cortex. *Nature* **420**, 812 (2002).
102. Xu, H. T., Pan, F., Yang, G. & Gan, W. B. Choice of cranial window type for in vivo imaging affects dendritic spine turnover in the cortex. *Nat. Neurosci.* **10**, 549–551 (2007).
103. Hatashita, S. & Hoff, J. T. The effect of craniectomy on the biomechanics of normal brain. *J. Neurosurg.* **67**, 573–578 (1987).
104. Schaller, B. *et al.* Hemodynamic and metabolic effects of decompressive hemicraniectomy in normal brain: An experimental PET-study in cats. *Brain Res.* **982**, 31–37 (2003).
105. Lam, M. A. *et al.* The ultrastructure of spinal cord perivascular spaces: Implications for the circulation of cerebrospinal fluid. *Sci. Rep.* **7**, 1–13 (2017).
106. Berliner, J. *et al.* Abnormalities in spinal cord ultrastructure in a rat model of post-traumatic syringomyelia. *Fluids Barriers CNS* **17**, 1–10 (2020).
107. Liu, J. *et al.* Energy dissipation in mammalian collagen fibrils: Cyclic strain-induced damping, toughening, and strengthening. *Acta Biomater.* **80**, 217–227 (2018).
108. Haut, R. C. & Little, R. W. A constitutive equation for collagen fibers. *J. Biomech.* **5**, 423–430 (1972).
109. Van Oosten, A. S. G. *et al.* Uncoupling shear and uniaxial elastic moduli of semiflexible biopolymer networks: Compression-softening and stretch-stiffening. *Sci. Rep.* **6**, 1–9 (2016).
110. Vahabi, M. *et al.* Elasticity of fibrous networks under uniaxial prestress. *Soft Matter* **12**, 5050–5060 (2016).
111. Storm, C., Pastore, J. J., MacKintosh, F. C., Lubensky, T. C. & Janmey, P. A. Nonlinear elasticity in biological gels. *Nature* **435**, 0–3 (2005).
112. Costanzo, F. & Miller, S. T. An arbitrary Lagrangian–Eulerian finite element formulation for a poroelasticity problem stemming from mixture theory. *Comput. Methods Appl. Mech. Eng.* **323**, 64–97 (2017).
113. Coussy, O. *Mechanics and physics of porous solids.* (John Wiley & Sons, 2011).
114. Bowen, R. M. Incompressible porous media models by use of the theory of mixtures. *Int. J. Eng. Sci.* **18**, 1129–1148 (1980).
115. Sánchez, A. L. *et al.* On the bulk motion of the cerebrospinal fluid in the spinal canal. *J. Fluid Mech.* **841**, 203–227 (2018).
116. Keith Sharp, M., Carare, R. O. & Martin, B. A. Dispersion in porous media in oscillatory flow between flat plates: Applications to intrathecal, periarterial and paraarterial solute transport in the central nervous

- system. *Fluids Barriers CNS* **16**, 1–17 (2019).
117. Heil, M. & Bertram, C. D. A poroelastic fluid-structure interaction model of syringomyelia. *J. Fluid Mech.* **809**, 360–389 (2016).
  118. Chou, D., Vardakis, J. C., Guo, L., Tully, B. J. & Ventikos, Y. A fully dynamic multi-compartmental poroelastic system: Application to aqueductal stenosis. *J. Biomech.* **49**, 2306–2312 (2016).
  119. von Holstein-Rathlou, S., Petersen, N. C. & Nedergaard, M. Voluntary running enhances glymphatic influx in awake behaving, young mice. *Neurosci. Lett.* **662**, 253–258 (2018).
  120. Xie, L. *et al.* Sleep drives metabolite clearance from the adult brain. *Science (80- )*. **342**, 373–377 (2013).
  121. Yang, L. *et al.* Evaluating glymphatic pathway function utilizing clinically relevant intrathecal infusion of CSF tracer. *J. Transl. Med.* **11**, 1–9 (2013).
  122. Nimmerjahn, A., Mukamel, E. A. & Schnitzer, M. J. Motor Behavior Activates Bergmann Glial Networks. *Neuron* **62**, 400–412 (2009).
  123. Dombeck, D. A., Khabbaz, A. N., Collman, F., Adelman, T. L. & Tank, D. W. Imaging Large-Scale Neural Activity with Cellular Resolution in Awake , Mobile Mice. 43–57 (2007).  
doi:10.1016/j.neuron.2007.08.003
  124. Huo, B.-X., Smith, J. B. & Drew, P. J. Neurovascular Coupling and Decoupling in the Cortex during Voluntary Locomotion. *J. Neurosci.* **34**, 10975–10981 (2014).
  125. Lamme, V. A., Zipser, K. & Spekreijse, H. Figure-ground activity in primary visual cortex is suppressed by anesthesia. *Proc. Natl. Acad. Sci. U. S. A.* **95**, 3263–8 (1998).
  126. Alkire, M. T., Hudetz, A. G. & Tononi, G. Consciousness and Anesthesia NIH Public Access. *Science (80- )*. **322**, 876–880 (2008).
  127. Aksenov, D. P., Li, L., Miller, M. J., Iordanescu, G. & Wyrwicz, A. M. Effects of anesthesia on BOLD signal and neuronal activity in the somatosensory cortex. *J. Cereb. Blood Flow Metab.* **35**, 1819–1826 (2015).
  128. Andrea Pisauro, M., Dhruv, N. T., Carandini, M. & Benucci, A. Fast hemodynamic responses in the visual cortex of the awake mouse. *J. Neurosci.* **33**, 18343–18351 (2013).
  129. Gakuba, C. *et al.* General anesthesia inhibits the activity of the ‘glymphatic system’. *Theranostics* **8**, 710–722 (2018).
  130. Bergel, A., Deffieux, T., Demené, C., Tanter, M. & Cohen, I. Local hippocampal fast gamma rhythms precede brain-wide hyperemic patterns during spontaneous rodent REM sleep. *Nat. Commun.* **9**, (2018).
  131. Nedergaard, M. Neuroscience. Garbage truck of the brain. *Science* **340**, 1529–30 (2013).
  132. Kudo, T. *et al.* Are cerebrovascular factors involved in Alzheimer’s disease? *Neurobiol. Aging* **21**, 215–224 (2000).
  133. la Torre, J. C. Alzheimer disease as a vascular disorder: nosological evidence. *Stroke* **33**, 1152–1162 (2002).
  134. Iadecola, C. Neurovascular regulation in the normal brain and in Alzheimer’s disease. *Nat. Rev. Neurosci.* **5**, 347–360 (2004).
  135. Ding, J. *et al.* Large perivascular spaces visible on magnetic resonance imaging, cerebral small vessel disease progression, and risk of dementia: The age, gene/environment susceptibility–Reykjavik study.

- JAMA Neurol.* **74**, 1105–1112 (2017).
136. Fernández, M. A., Formaggia, L., Gerbeau, J.-F. & Quarteroni, A. The derivation of the equations for fluids and structure. in *Cardiovascular Mathematics: Modeling and simulation of the circulatory system* (eds. Formaggia, L., Quarteroni, A. & Veneziani, A.) 77–121 (Springer Milan, 2009). doi:10.1007/978-88-470-1152-6\_3
  137. Wick, T. Fluid-structure interactions using different mesh motion techniques. *Comput. Struct.* **89**, 1456–1467 (2011).
  138. Gerbeau, J.-F., Vidrascu, M. & Frey, P. Fluid–structure interaction in blood flows on geometries based on medical imaging. *Comput. Struct.* **83**, 155–165 (2005).
  139. Eriksson, K., Estep, D., Hansbo, P. & Johnson, C. *Computational differential equations*. **1**, (Cambridge University Press, 1996).
  140. Guizar-Sicairos, M., Thurman, S. T. & Fienup, J. R. Efficient subpixel image registration algorithms. *Opt. Lett.* **33**, 156 (2008).
  141. Gao, Y. R. & Drew, P. J. Determination of vessel cross-sectional area by thresholding in Radon space. *J. Cereb. Blood Flow Metab.* **34**, 1180–1187 (2014).
  142. Lindquist, M. A., Loh, J. M., Atlas, L. Y. & Wager, T. D. Modeling the hemodynamic response function in fMRI: efficiency, bias and mis-modeling. *Neuroimage* **45**, S187–S198 (2009).
  143. Kong, L., Little, J. P. & Cui, M. Motion quantification during multi-photon functional imaging in behaving animals. *Biomed. Opt. Express* **7**, 3686 (2016).
  144. Glover, G. H. Deconvolution of impulse response in event-related BOLD fMRI. *Neuroimage* **9**, 416–429 (1999).
  145. Prevost, T. P., Balakrishnan, A., Suresh, S. & Socrate, S. Biomechanics of brain tissue. *Acta Biomater.* **7**, 83–95 (2011).
  146. COMSOL Multiphysics® v. 5.4. www.comsol.com. COMSOL AB, Stockholm, Sweden.
  147. MATLAB, version 9.7.0 (R2019b), The MathWorks Inc., Natick, Massachusetts (2019).
  148. Wolfram Research, Inc., Mathematica, Version 12.0, Wolfram Research Inc., Champaign, Illinois (2019).

## Supporting Information

**Figure S1** | When the brain is modeled as providing a rigid boundary to the PVS, a Navier-Stokes flow predicts negligible unidirectional flow and pressure differences large enough to clearly call into question the rigidity assumption.

- a. Plot of the fluid velocity induced in the PVS by the arteriolar pulsation. Contour showing the axial velocity (velocity in the z-direction) in a cross-section of the PVS. The colors indicate the direction and magnitude of flow. Fluid velocity vectors (arrows) show a parabolic flow profile, as is expected from a Navier-Stokes model. Heartbeat pulsations drive negligible unidirectional flow with a mean flow speed ( $\langle v_z \rangle$ ) of  $1.8 \times 10^{-3} \mu\text{m/s}$ . To make the movements clearly visible, we scaled the displacements by a factor of 10 in post-processing.

- b. Fluid pressure in the PVS corresponding to the flow shown in **a**. Pressure changes due to fluid flow in the PVS reach several mmHg. These pressures will deform the soft brain tissue, which has a shear modulus of 1-8 kPa<sup>52,145</sup> (8-60 mmHg). The dotted line shows the estimated deformation in the brain tissue (shear modulus 4kPa – Kirchhoff/De Saint-Venant elasticity with Poisson ratio of 0.45) from the pressure shown in the figure. Under these assumptions, the deformations in the brain tissue (0.08  $\mu\text{m}$ ) are in the same range as the peak of heartbeat driven pulsations (0.06  $\mu\text{m}$  – shown in Fig 1**a**). Therefore, the deformability of brain tissue cannot be neglected even if the PVS is considered as a non-porous fluid filled channel.

**Figure S2** | When the brain is modeled as providing a rigid boundary to the PVS, even when flow resistances are absent, one predicts negligible unidirectional flow with pressure differences large enough to call into question the rigidity assumption.

- a. Plot of the fluid velocity induced in the PVS by the arteriolar pulsation. Contour showing the axial velocity (velocity in the z-direction) in a cross-section of the PVS. The colors indicate the direction and magnitude of flow. Fluid velocity vectors (arrows) are provided to help the reader interpret the flow direction from the colors. Heartbeat pulsations drive negligible unidirectional flow with a mean flow speed( $-[v_z]$ ) of  $2.9 \times 10^{-3} \mu\text{m/s}$ . To make the movements clearly visible, we scaled the radial displacements by a factor of 10 in post-processing.
- b. Fluid pressure in the PVS corresponding to the flow shown in **a**. Pressure changes due to fluid flow in the PVS reach several mmHg. These pressures will deform the soft brain tissue, which has a shear modulus of 1-8 kPa<sup>52,145</sup> (8-60 mmHg). The dotted line shows the estimated deformation in the brain tissue (shear modulus 4kPa – Kirchhoff/De Saint-Venant elasticity with Poisson ratio of 0.45) from the pressure shown in the figure. Under these assumptions, the deformations in the brain tissue are 10 times bigger (0.71  $\mu\text{m}$ ) in magnitude compared the peak of heartbeat driven pulsations (0.06  $\mu\text{m}$  – shown in Fig 1**a**). This shows the deformability of brain tissue cannot be neglected.

**Figure S3** | Peristaltic pumping can occur in models with unphysiologically long PVS. These models predict physiologically impossible pressure changes in the PVS. Note the geometry is depicted with an unequal aspect ratio in the radial (r) and axial (z) directions for viewing convenience.

- a. Plot of the fluid velocity induced in the PVS by arteriolar pulsation in the non-compliant brain model, where the length of the PVS is equal to one wavelength of the peristaltic wave (0.1 m, see Table 1). Color in the PVS shows the axial velocity (velocity in the z-direction) in a cross section of the PVS throughout the pulsation cycle. Fluid velocity vectors (arrows) are provided to help the reader interpret the flow direction from the colors. Heartbeat pulsations can drive unidirectional flow with a mean flow speed( $-[v_z]$ ) of  $143.2 \mu\text{m/s}$ , but this would be accompanied by large velocity oscillations in the range of 20,000  $\mu\text{m/s}$  and large pressure changes in the range of 200,000 mmHg. Note: Arteriolar and brain tissue displacements induced by arteriolar pulsations are very small ( $<0.1 \mu\text{m}$ ). To make the movements clearly visible, we scaled the radial displacements by 10 times in post-processing.
- b. Plot of the pressure induced in the PVS by arteriolar pulsation in the non-compliant brain model, where the length of the PVS is equal to one wavelength of the peristaltic wave (0.1m, see Table 1). No pressure

is applied at both ends of the PVS. Color in the PVS shows the pressure in a cross section of the PVS throughout the pulsation cycle.

**Figure S4|** Pulsation-induced fluid flows in the PVS are small in an incompressible Neo-Hookean brain model. Note the geometry is depicted with an unequal aspect ratio in the radial (r) and axial (z) directions for viewing convenience.

- a. The imposed heartbeat-driven pulsations in arteriolar radius ( $\pm 0.5\%$  of mean radius<sup>16</sup>,  $R_i$ ) at 10 Hz, the heartrate of an un-anesthetized mouse. The pulse wave travels at 1 meter per second along the arteriolar wall, into the brain<sup>58,59</sup>
- b. Colors showing the axial velocity (velocity in the z-direction) in a cross section of the PVS, when the arteriolar wall movement is given by periodic pulsations. Fluid velocity vectors (arrows) are provided to help the reader interpret the flow direction from the colors. The white region is stationary. These plots (compare to those in Fig 3c) show that there is no significant flow into the PVS driven by arteriolar pulsations. Note: Arteriolar and brain tissue displacements induced by arteriolar pulsations are very small ( $< 0.1 \mu\text{m}$ ). To make the movements clearly visible, we scaled the radial displacements by 10 times in post-processing.
- c. Flow out of the PVS and into the subarachnoid space, through the pial opening of the PVS. The flow rates predicted by the model with nearly incompressible (Poisson's ratio of 0.45) (magenta) and a completely incompressible, Neo-Hookean models (blue) were nearly identical.

**Figure S5|** Pulsation-driven flows are small in simulations when the subarachnoid space (SAS) is modeled as a porous, fluid-filled region. Note the geometry is depicted with an unequal aspect ratio in the radial (r) and axial (z) directions for viewing convenience.

- a. Schematic showing the model of the penetrating arteriole used in this simulation. The brain tissue is modelled as a compliant solid. Subarachnoid space is modelled as a fluid filled region (SAS "geometry" model).
- b. Schematic showing the alternative model of the penetrating arteriole (same as Fig 3a). The Subarachnoid space is modelled as a flow resistance ( $R_s$ ) at the end of the PVS (SAS "resistance" model). The results for the SAS "resistance" model are shown in Fig 3.
- c. The imposed heartbeat-driven pulsations in arteriolar radius ( $\pm 0.5\%$  of mean radius<sup>16</sup>,  $R_i$ ) at 10 Hz, the heartrate of an un-anesthetized mouse. The pulse wave travels at 1 meter per second along the arteriolar wall, into the brain.
- d. Plot showing the axial velocity (velocity in the z-direction) in a cross section of the PVS and the connected SAS, when the arteriolar wall movement is given by periodic pulsations. Fluid velocity vectors (arrows) are provided to help the reader interpret the flow direction from the colors. Because the fluid is incompressible, the flow speed decreases when flowing into the SAS, which has a larger area of cross section compared to the PVS. The region in white has little to no flow. These plots show that there is no significant flow into the PVS driven by arteriolar pulsations. Note: Arteriolar and brain tissue

displacements induced by arteriolar pulsations are very small ( $<0.1 \mu\text{m}$ ). To make the movements clearly visible, we scaled the displacements by 10 times in post-processing.

- e. Plot of the fluid flow through the top face of the PVS into the SAS. The flow rates predicted by the SAS “resistance” model (magenta) and the SAS “geometry” model (blue) are very similar.

**Figure S6|** Deformation of the brain tissue due to the pressure changes in the PVS. Note the geometry is depicted with an unequal aspect ratio in the radial (r) and axial (z) directions for viewing convenience.

- a. Radial displacement contours in the brain tissue (maximum deformation, occurs at 1.16 seconds for the vasodilation profile shown in b). The brain tissue can deform by upto  $1.2 \mu\text{m}$ , when the arteriole (with an initial radius of  $12\mu\text{m}$ ) increases its radius by  $1.8 \mu\text{m}$ .
- b. Plot shows the change of radial displacement at the PVS-Brain interface with time. These deformations can be explained by the pressure changes in the PVS. When there is fluid outflow from the PVS, the increase in the pressure causes the brain tissue to deforms radially outward and when there is fluid influx, the brain tissue deforms radially inward. The smallest tissue displacement is at the pial surface ( $z = 250\mu\text{m}$ ), which is the location of smallest pressure changes, as it is connected to the SAS flow resistance. The brain tissue is fixed at  $r=150\mu\text{m}$ .
- c. Plot shows the change of radial displacement in the brain tissue at different distances from the centerline of the vessel.

**Figure S7|** Vasodilation-induced PVS fluid flow in a completely incompressible, Neo-Hookean model was very similar to the compressible SVK model. Note the geometry is depicted with an unequal aspect ratio in the radial (r) and axial (z) directions for viewing convenience.

- a. Plot of the prescribed arteriolar wall movement, which is identical to the one shown in Fig 4a.
- b. Plot showing the axial (z-direction) fluid velocity a cross section of the PVS, when the arteriolar wall movement is given by neural activity-driven vasodilation. A portion of the vessel lumen is shown in red to provide a sense of vasodilation. Fluid velocity vectors (arrows) are provided to help the reader interpret the flow direction from the colors. The region in white has little to no flow. These plots (very similar to the ones in Fig 4a) show that compared to heartbeat-driven pulsations (supp Fig 3b), vasodilation-driven fluid flow occurs through the entire length of the PVS and has substantially higher flow velocities.
- c. Flow out of the PVS and into the pia, through the top face of the PVS. The flow rates predicted by the model with nearly incompressible (SVK model with Poisson’s ratio of 0.45) brain tissue (magenta) and a completely incompressible, Neo-Hookean model (blue) are very similar.

**Figure S8|** Arteriolar dilations during functional hyperemia drive fluid exchange between the PVS and SAS in the SAS “geometry” model. Note the geometry is depicted with an unequal aspect ratio in the radial (r) and axial (z) directions for viewing convenience.

- a. The arteriolar wall movement is prescribed by a typical neural activity-driven vasodilation response, the same one shown in Fig 4a.

- b. Plot showing the axial velocity (velocity in the z-direction) in a cross section of the PVS and the connected SAS, when the arteriolar wall movement is given by neural activity-driven vasodilation. A portion of the vessel lumen is shown in red to provide a sense of vasodilation. Fluid velocity vectors (arrows) are provided to help the reader interpret the flow direction from the colors. Because the fluid is incompressible, the flow speed decreases when flowing into the SAS, which has a larger area of cross section compared to the PVS. The region in white has little to no flow. These plots (very similar to the ones in Fig 4a) show that compared to heartbeat-driven pulsations (supp Fig 3b), vasodilation-driven fluid flow occurs through the entire length of the PVS and has substantially higher flow velocities. Note that the scale for the radial direction is different than that in the axial direction.
- c. Flow out of the PVS and into the pia, through the top face of the PVS. The flow rates predicted by the SAS “resistance” model (magenta) and the SAS “geometry” model (blue) are almost identical.

**Figure S9|** Vasodilation drives orders of magnitude higher fluid exchange between the PVS and subarachnoid space compared to heartbeat driven pulsations. The plots show the changes in fluid exchange percentage, the percentage of fluid in the PVS exchanged with the SAS, with change of model parameters. The model predicts that compared to arteriolar pulsations; the vasodilation driven fluid exchange percentage is two orders of magnitude higher. This difference is similar for different values of elastic modulus of the brain (a), the width of the PVS (b) and the fluid permeability of the PVS (c). In (c), when the permeability is infinite, Darcy-Brinkman’s law transforms into Navier-Stokes’ law for fluid flow. All the plots are made on a log-log scale because the parameters were changed by 1-3 orders of magnitude.

**Figure S10|** Heartbeat drives 0.5-4% (peak-to-peak) changes in arteriolar diameter.

- a. Sample image of the in-vivo fluorescence measured by two-photon microscopy following intravenous injection of FITC conjugated dextran (150 kDa) shows the cerebral vasculature near the surface of the brain (scale bar = 25  $\mu\text{m}$ ). Inset (scale bar = 10 $\mu\text{m}$ ) shows a smaller region containing a segment of the arteriole, that is scanned at 30Hz to obtain arteriolar diameter changes in the typical heartrate frequencies (4-14 Hz).
- b. Sample plot of the diameter values measured for the arteriole shown in **a**. The plot shows that heartbeat drives 1.4% peak-to-peak change in diameter for this arteriole.
- c. Spectrogram shows the log power of diameter changes for the sample arteriole shown in **a**. There is a clear peak in spectral power at 5.59 Hz, which is the frequency of the heartbeat.
- d. Scatter plot shows the relation between the percentage changes in diameter (8 vessels, 6 mice) and the mean diameter at heartrate frequencies. To measure the pulsations in arterioles (diameter <40  $\mu\text{m}$ ), we had to anesthetize the mice (green). The pulsations in awake animals could only be measured in large arteries (blue). Isoflurane anesthesia helped with reducing motion artifacts in measuring the small magnitude pulsations. No statistical tests were performed between the anesthetized and awake data due to the small sample size.

**Figure S11|** The presence of deformable brain tissue makes the PVS more resistant to fluid flow changing at high frequency.

- a. Geometry for a model in which the brain is a rigid boundary to the PVS (top) and the equivalent circuit diagram. The driver for fluid flow is the arteriolar wall motion. The flow resistance of the PVS can be modelled by a simple resistor is independent of the frequency of the arteriolar wall movement.
- b. Geometry for the fluid-structure interaction model with a deformable brain(top) and the equivalent circuit diagram. The driver for fluid flow is the arteriolar wall motion. The total flow resistance of the system can be modelled by a resistance from the PVS and an inductance because of the deformable tissue. In this model, the flow resistance of the system increases with increase in the frequency of the arteriolar wall motion. This means that for arteriolar wall motion at high frequency, less fluid will be exchanged between the PVS and the SAS.
- c. Plot shows the relation between fluid exchange percentage and frequency of arteriolar wall motion. The arteriolar wall motion was given by a 4% peak-peak sinusoidal wave with different frequency values. The default values were used for all other parameters (see Table 1). For very low frequencies ( $<0.1$  Hz), the fluid exchange driven by the arteriolar wall is same whether or not brain deformability is taken into account.. For higher frequencies, the fluid exchange percentage has an inverse power law relation with the frequency of arteriolar wall motion.

**Figure S12|** The lack of negative radial displacement in the brain tissue can be attributed to the non-linear elastic response of the connective tissue in the PVS

- a. The connective tissue in the PVS is possibly made up of extracellular matrix fibers (collagen) and fibroblasts.
- b. When arterioles dilate, the connective tissue is under compression (middle) and the fibers buckle (bend) rather than compress due to the low energy cost of bending. Therefore, there are very low elastic forces and our assumption that the forces in the PVS originate mainly from the fluid pressure is valid.
- c. When the arterioles constrict or return to their original size, the connective tissue is in tension and the fibers stretch, creating significantly larger elastic forces. In this case, our assumption that the forces in the PVS originate mainly from the fluid pressure does not hold and the fluid-structure interaction model cannot predict the behavior accurately.

**Figure S13|** The procedure for measuring brain tissue displacement from in-vivo imaging data collected with a two-photon laser scanning microscope.

- a. Flow chart depicting the complete procedure used to calculate displacements in the brain tissue. The procedure can be broken down into 4 major sub-sections as shown in the figure. For a full description of the procedure, see methods.
- b. A depiction of the iterative method in calculating displacements. The figure on the left shows a reference image. The intensity is shown by a Parula colormap (Matlab). The images on the right show two cases of displaced images. The one on the top is rotated by  $2^\circ$ , and can be matched to the reference image (shown in gray) by a simple displacement. After the first calculation of the displacement and correcting the displaced image, the reference and the displaced image match and further iterations of displacement calculation yield a zero value, showing that the displacement calculation has converged. The one on the bottom is rotated by  $45^\circ$ , and cannot be matched to the reference image (shown in gray)

by a simple displacement. In this case, every iteration of displacement calculation yields a non-zero value and the calculation is not converged.

**Figure S14** | The displacement calculation method is robust to noise.

- A computer generated image (512x512 pixels) with randomly oriented lines.
- The radially-outward displacement given to the image shown in **a**.
- An image showing the radially-outward displacement at peak displacement (frame number 13). The initial position of the lines is shown in white and the displaced position is shown in blue.
- The displacement extraction procedure (shown in Supplementary figure 12) is robust to noise and predicts correct displacement. On the left, a case with low signal-to-noise ratio (0.59) is shown. The calculated displacements are very close to the actual displacement. The accuracy is comparable to the case with high signal-to-noise ratio (4.14) on the right. However, high noise results in a detection of displacement at fewer locations. The plot in the center shows that at low signal to noise ratio only 30% of the possible locations can be used for displacement calculations. Signal-to-noise ratio is calculated as the ratio of the mean signal value to the standard deviation in the noise. **Movie SV1:**  
SV1\_heartbeat\_50s.avi; Particle tracking simulation for heartbeat driven pulsations. Duration: 50s

**Movie SV2:** SV2\_vasodilation\_50s.avi; Particle tracking simulation for functional hyperemia. Duration: 50s.

**Movie SV3:** SV3\_Sample\_dilation.avi; Sample imaging data showing blood vessel and brain tissue displacement. Brain tissue is marked in green (Thy1-YFP). Blood vessels are marked in magenta (Texas Rd).

**Appendix:** Appendix.pdf; Full mathematical formulation of the initial-boundary value problems in arbitrary Lagrangian-Eulerian coordinates.

## Figures

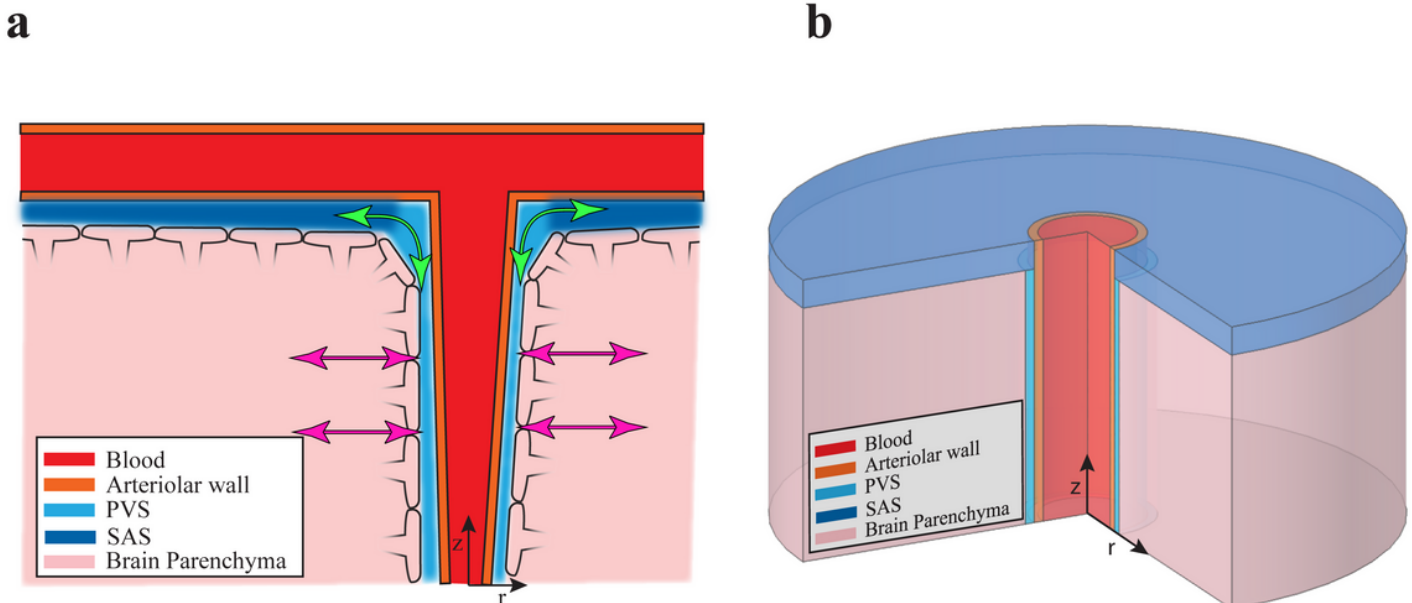


**Figure 1**

Schematic of the anatomical structure of a penetrating arteriole and surrounding tissue a. Depiction the fluid filled PVS between the arteriolar wall and the brain parenchyma, adapted from Abbot et al10. The glia limitans covers the surface of the brain tissue and forms the brain-PVS interface. The subarachnoid space (SAS) and paravascular spaces (PVS) are interconnected fluid-filled compartments. The low resistance pathway for fluid flow to and from the PVS (along the SAS) is shown in green, while the high resistance pathway (through the brain parenchyma) is shown in magenta. Our simulations only look at fluid movement through the green pathway. b. Geometry of the computational model of a penetrating arteriole and the brain and fluid around it. The model is cylindrically symmetric around the penetrating arteriole, allowing us to use axisymmetric simulations (see appendix for full mathematical detail).

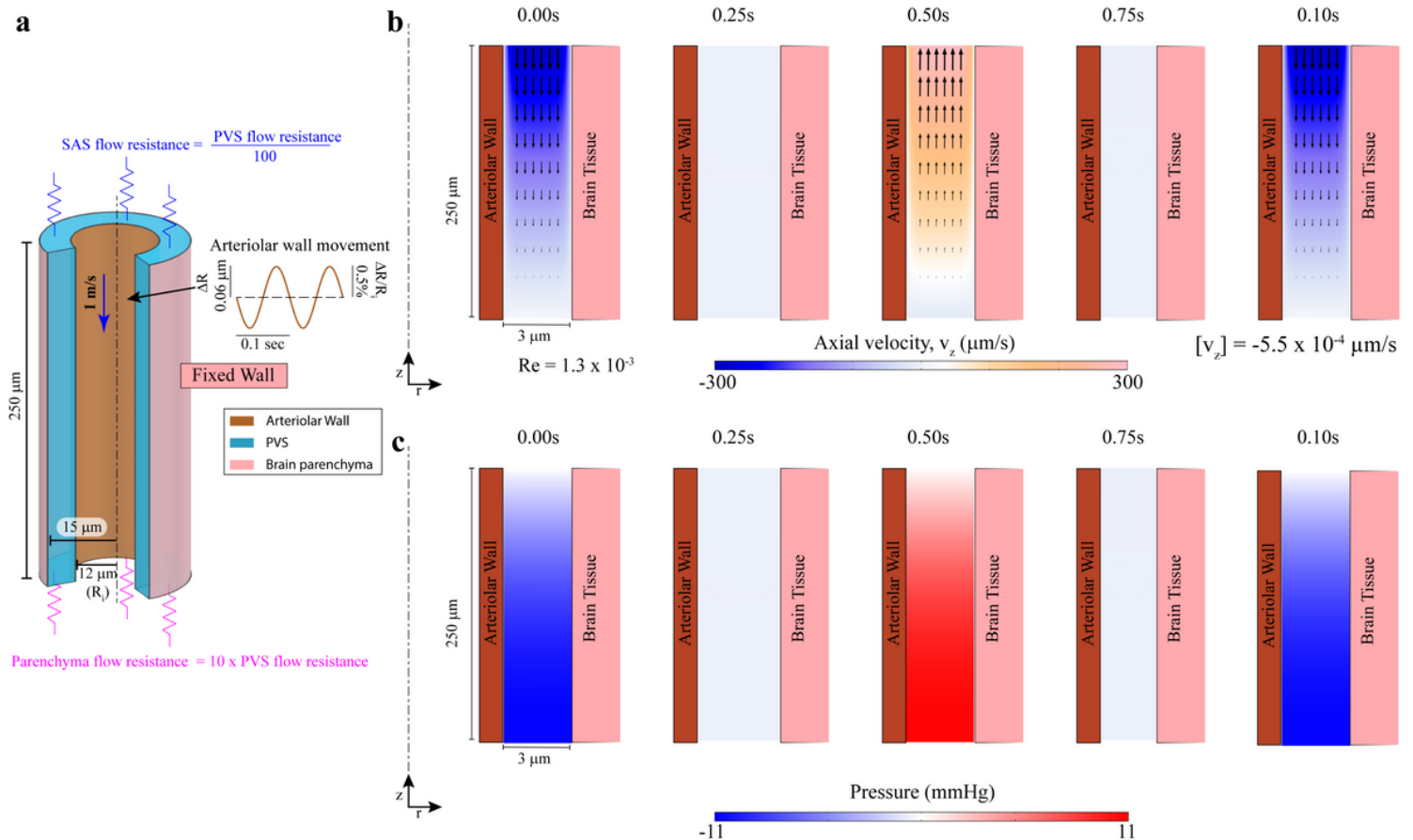


**Figure 2**

Modeling fluid flows and induced pressures while ignoring brain deformability. Note the geometry is depicted with an unequal aspect ratio in the radial (r) and axial (z) directions for viewing convenience. a. Geometry of the PVS in our model. The outer wall of the arteriole is shown in dark orange and the boundary of the brain parenchyma is shown in pink. The dashed line represents the centerline of the arteriole. The inset shows the imposed heartbeat-driven pulsations in arteriolar radius ( $\pm 0.5\%$  of mean radius  $16, R_i$ ) at 10 Hz, the heartrate of an un-anesthetized mouse. The pulse wave travels at 1 meter per second along the arteriolar wall, into the brain<sup>58,59</sup> (blue arrow). The flow through the SAS and the Brain Parenchyma was modelled by flow resistances (shown in blue and magenta respectively). In b and c, a cross section of the PVS is shown

together with the surrounding arteriolar wall (on the left) and brain tissue (on the right). b. Plot of the fluid velocity induced in the PVS by the arteriolar pulsation. Contour showing the axial velocity (velocity in the z-direction) in a cross-section of the PVS. The colors indicate the direction and magnitude of flow. Fluid velocity vectors (arrows) are provided to help the reader interpret the flow direction from the colors. Heartbeat pulsations drive negligible unidirectional flow with a mean flow speed ( $-[v_z]$ ) of  $5.5 \times 10^{-4} \mu\text{m/s}$ . To make the movements clearly visible, we scaled the displacements by a factor of 10 in post-processing. c. Fluid pressure in the PVS corresponding to the flow shown in b. Pressure changes due to fluid flow in the PVS reach several mmHg. These pressures will deform the soft brain tissue, which has a shear modulus of 1-8 kPa (8-60 mmHg). The dotted line shows the estimated deformation in the brain tissue (shear modulus 4kPa – Kirchhoff/De Saint-Venant elasticity with Poisson ratio of 0.45) from the pressure shown in the figure. Under these assumptions, the deformations in the brain tissue are 60 times bigger ( $3.59 \mu\text{m}$ ) in magnitude compared the peak of heartbeat driven pulsations ( $0.06 \mu\text{m}$  – shown on inset in a). Therefore, the deformability of brain tissue cannot be neglected.

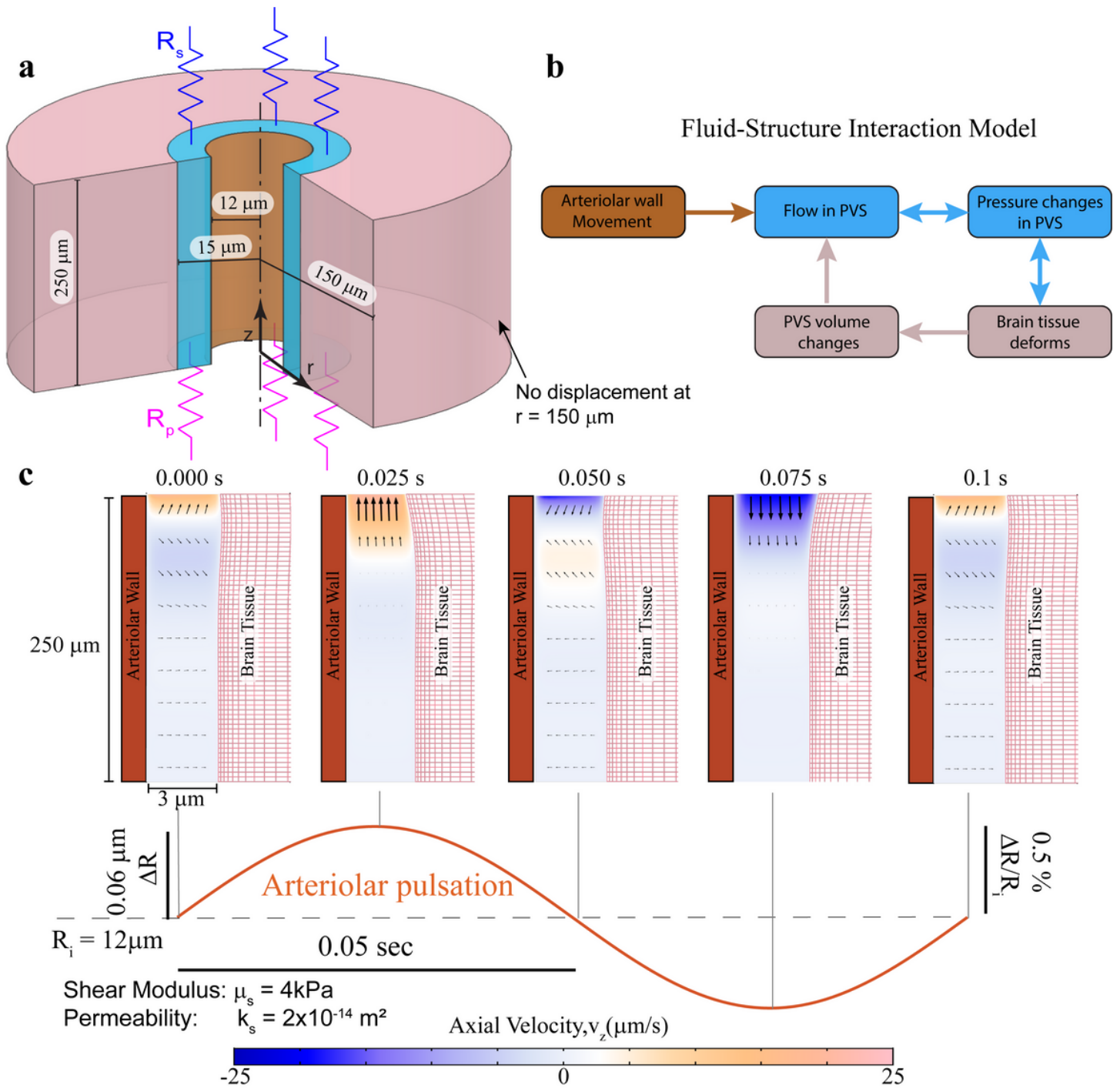


**Figure 3**

Arteriolar pulsations do not drive flow in the PVS in an arteriolar-brain model with realistic mechanical properties. Note the geometry is depicted with an unequal aspect ratio in the radial ( $r$ ) and axial ( $z$ ) directions for viewing convenience. a. The model of the penetrating arteriole. The brain tissue is modelled as a compliant solid. The subarachnoid space is modelled as a flow resistance ( $R_s$ ) at the pial end of the PVS and the parenchyma is modelled as a flow resistance ( $R_p$ ) at the other end. For the simulation with the subarachnoid space modelled as a fluid filled region, see Fig S5. b. A schematic depicting the fluid-structure interaction model described in a. The arteriolar wall movement drives the fluid movement in the PVS. This fluid movement is coupled with the pressure changes. These pressure changes deform the brain tissue,

changing the shape and volume of the PVS. These volume changes will affect the flow in the PVS, as demonstrated in c. c. Plot showing the axial fluid velocity (velocity in the z-direction) in a cross section of the PVS, when the arteriolar wall movement is given by periodic pulsations. The amplitude and frequency of the arteriolar pulsations are taken to be typical values for cerebral arterioles in mice. Fluid velocity vectors (arrows) are provided to help the reader interpret the flow direction from the colors. The region in white has little to no flow. These plots show that there is no significant flow into the PVS driven by arteriolar pulsations. Note: Arteriolar and brain tissue displacements induced by arteriolar pulsations are very small ( $<0.1 \mu\text{m}$ ). To make the movements clearly visible, we scaled the displacements by a factor of 10 in post-processing. These calculations were performed with fluid permeability,  $k_s = 2 \times 10^{-14} \text{ m}^2$  and tissue shear modulus  $\mu_s = 4 \text{ kPa}$ . The fluid exchange percentage for a wide range of parameter values is shown in Fig S9.

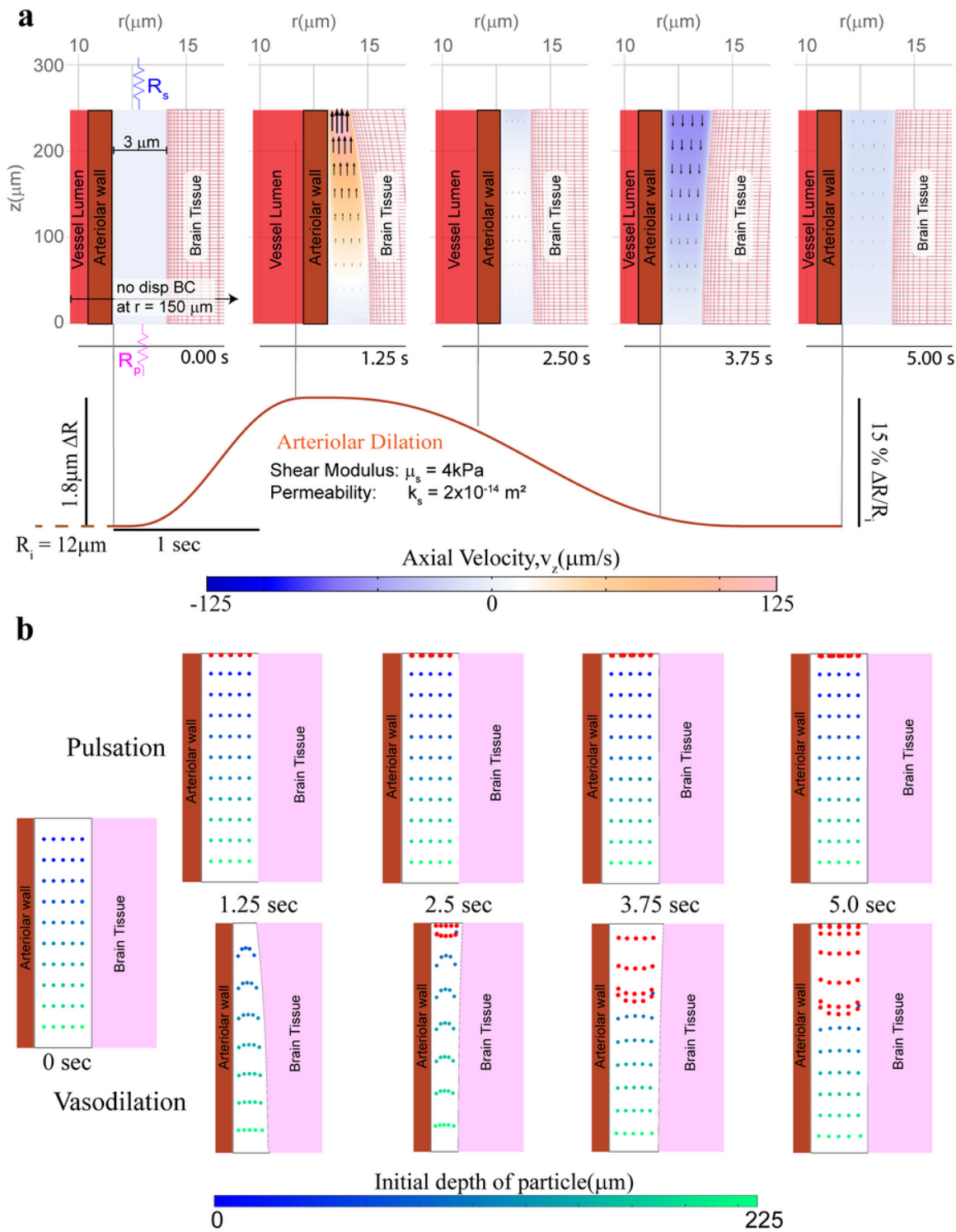


**Figure 4**

Arteriolar dilations during functional hyperemia can drive fluid exchange in the PVS. Note the geometry is depicted with an unequal aspect ratio in the radial ( $r$ ) and axial ( $z$ ) directions for viewing convenience. a. Contours showing the axial velocity (velocity in the  $z$ -direction) in a cross section of the PVS, when the arteriolar wall movement is given by a typical neural activity-driven vasodilation response. The boundary conditions (shown in the left panel) for this simulation are the same as the ones shown in Fig 3. Compared to heartbeat-driven pulsations (Fig 3c), vasodilation-driven fluid flow occurs through the entire length of the

PVS and has substantially higher flow velocities. The model also predicts that the vasodilation can also cause significant deformation in the brain tissue. A portion of the vessel lumen is shown in red to provide a sense of vasodilation. **b.** Comparison of particle motion in the fluid of the PVS during arteriolar pulsations and vasodilation. The blue-green dots represent fluid in the PVS, with the colormap showing the initial position (depth) of the fluid particle in the PVS. Fluid particles near the SAS (red dots) are added once every 0.5 secs to the simulation to simulate fluid mixing between the PVS and the SAS. There is very little fluid movement driven by arteriolar pulsations. Vasodilation drives appreciable fluid exchange between the PVS and the SAS. These calculations were performed with fluid permeability,  $k_s = 2 \times 10^{-14} \text{ m}^2$  and tissue shear modulus  $\mu_s = 4 \text{ kPa}$ . The fluid exchange percentage for a wide range of parameter values is shown in Fig S9.

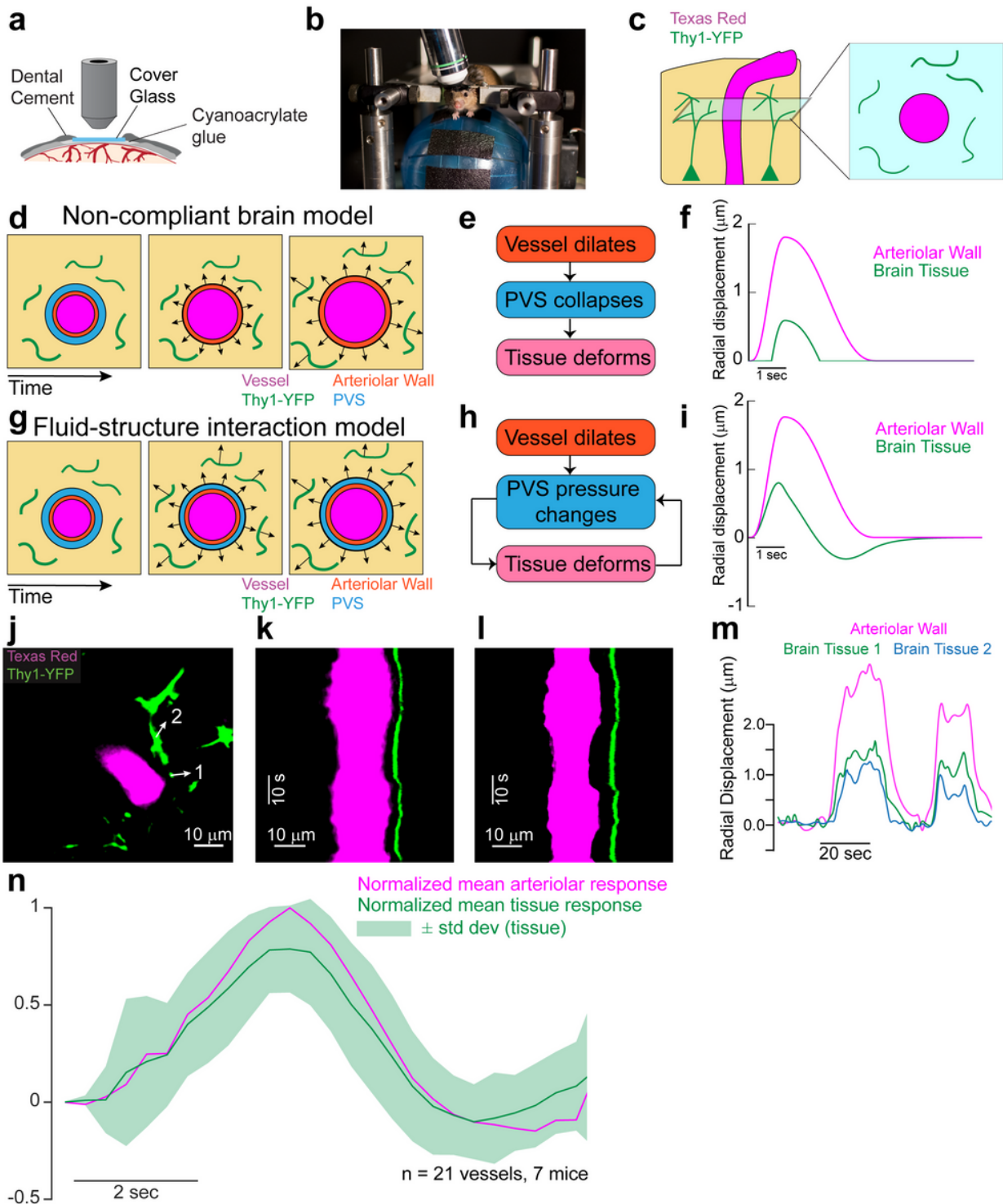


## Figure 5

A schematic of the expected brain tissue deformation from a fluid-structure interaction model. Here the pressure changes in the PVS cause the brain tissue to deform. h. Flow chart of the mechanism of brain tissue deformation in a fluid-structure interaction model. i. The expected radial displacement in the brain tissue in response to arteriolar dilation in the fluid-structure interaction model (also see Fig S6). Note that the expected values are based on the displacement used for our simulations and actual values may vary. j. Median frame of the 2D image collected during in-vivo imaging. Example image of penetrating arteriole(magenta) and YFP expressing neurons(green). The arrows show the direction of the displacement measured at the location indicated by the tail of the arrow. k, l. Projection in time along a line running through the arrows 1 and 2 respectively shown in j. The images show that when the vessel dilates (indicated by a widening of the vessel in magenta), there is a corresponding radially-outward deformation in the brain tissue (indicated by the movement of the green line). Time moves forward in the in the vertically downward direction in both images. m. The calculated radial displacement in the brain tissue in response to changes in arteriolar radius. The data suggests that the brain tissue deforms due to pressure changes in the PVS before the PVS completely collapses. n. The average (7 mice, 21 vessels) peak-normalized impulse response of the radial displacement of the arteriolar wall (magenta) compared to the average peak-normalized impulse response of the radial displacement in the brain tissue (only one data point per vessel was used for this calculation). The data shows that there is no delay between displacement of arteriolar wall and the tissue, suggesting that the brain tissue deforms due to pressure changes in the PVS as predicted by the fluid-structure interaction model.

## Supplementary Files

This is a list of supplementary files associated with this preprint. Click to download.

- [FigS9paramsweep.tif](#)
- [FigS10pulsationmeasurement.tif](#)
- [FigS11Frequencyresponse.tif](#)
- [FigS12Fibers.tif](#)
- [FigS14psuedodata.tif](#)
- [Appendix.pdf](#)
- [FigS1rigidflows.tif](#)
- [FigS2rigidflownorobin.tif](#)
- [FigS3rigidfulllength.tif](#)
- [FigS4pulsationsincompressible.tif](#)
- [FigS5pulsationsSAS.tif](#)
- [FigS6displacements.tif](#)
- [FigS7vasodilationincompressible.tif](#)
- [FigS8vasodilationSAS.tif](#)

- FigS12Collagen.tif
- FigS13flowchart.tif
- SV1heartbeat50s.avi
- SV2vasodilation50s.avi
- SV3Sampledilation.avi
- Methods.pdf